Supplementary Information:

Operando laboratory XAS of Ni nanoparticles in CO_2 methanation using a plug-flow fixed-bed cell with von Hámos spectrometer

Sebastian Praetz,[*a‡] Emiliano Dal Molin,[b‡] Delf Kober,[b] Marko Tesic,[a] Christopher Schlesiger,[a] Peter Kraus,[c] Julian T. Müller,[b] Jyothilakshmi Ravi Aswin,[d] Daniel Grötzsch,[a] Maged F. Bekheet,[b] Albert Gili,[e] Aleksander Gurlo,[b] and Birgit Kanngießer[a]

[a] *Technische Universität Berlin, Institute of Physics and Anstronomy, Sekr. EW 3-1, Hardenbergstraße 36, 10623 Berlin, Germany. E-mail: sebastian.praetz@tu-berlin.de*

[b] *Technische Universität Berlin, Chair of Advanced Ceramic Materials, Hardenbergstr. 40, 10623 Berlin, Germany.*

[d] *Technische Universität Berlin, Conductivity and Catalysis Lab, Hardenbergstr. 40, 10623 Berlin, Germany.*

[d] *Helmholtz-Zentrum Berlin, Department Atomic-Scale Dynamics in Light-Energy Conversion, 14109 Berlin, Germany.*

[e] *Helmholtz-Zentrum Berlin für Materialien und Energie, 14109 Berlin, Germany.*

‡ These authors contributed equally to this work

This is the Electronic Supplementary Information for the work with the title "Operando laboratory XAS of Ni nanoparticles in CO_2 methanation using a plug-flow fixed-bed cell with von Hámos spectrometer".

Contents

1 Experimental details

This section provides extended details supporting the main text methods. The laboratory von Hámos spectrometer (Section 1.1) was combined with an IR-furnace capillary reactor cell (Section 1.2) adapted from Bischoff *et al.* [1] Gas analysis was performed using online GC (Section 1.3). Catalyst synthesis, reference materials, and additional samples are described in Section 2.

1.1 Laboratory von Hámos spectrometer

The measurements were performed using a self-developed wavelength-dispersive von Hámos spectrometer previously described by Schlesiger *et al.* [2,3] Key components include a micro-focus X-ray tube MCBI 50B-70 Mo optimised to 15 kV (30 W at 15 kV, rtw RÖNTGEN-TECHNIK DR. WARRIKHOFF GmbH & Co. KG), a cylindrically bent HAPG mosaic crystal (Optigraph GmbH) optimized for XANES with short acquisition times, and an EIGER2 R 500K detector (512 × 1030 pixels, 75 µm pitch, DECTRIS) (Fig. S1). The evacuated beam path (5 mbar) uses 25 µm Kapton windows to minimize air absorption.

The modified von Hámos geometry aligns the detector perpendicular to the central beam, enabling broader spectral bandwidth than classical designs. [4] Different energies probe distinct sample regions (meridional plane), requiring homogeneous samples and differential conversion conditions to avoid artefacts from composition gradients. Non-flat geometries (e.g., cylindrical capillaries) cause spectral distortions due to sagittal plane effects; detailed analysis is provided by Schlesiger. [5]

The energy band-pass of approximately 500 eV for the optic used in this study – reflecting the simultaneously measured energy range – is determined by the Bragg angle of the HAPG crystal. Optics with different dimensions or bending radii exhibit distinct energy band-passes. For a detailed description of the optical design and performance, see the works of Schlesiger *et al.* [2,3,5]

The probed area scales with energy (few mm^2 at Ni K-edge) and decreases at higher energies. [2] *Ex situ* samples use powder on adhesive tape ($1\times1\,cm^2$) or Ø13 mm pellets; preparation follows Praetz and Schlesiger *et al.* [6] Capillaries (1.0/0.8 mm OD/ID, CM Scientific) are measured vertically to maximize sagittal signal despite meridional distortions from cylindrical geometry.

Transmission spectra $\mu(E)Q$ require sample (I_d) and empty (I_0) measurements. For capillary measurements, I_0 is recorded without an empty capillary. The SiC tube slit (4×1 mm) and adjustable entrance slit (essential for capillary measurements) restrict the probed region precisely to the 0.8 mm capillary interior.

Since the capillary does not cover the entire measurable sample area – further limited by the SiC tube 1 mm slit (see Section 1.2) – the adjustable slit is essential (see Fig. 1(c)). Due to the HAPG mosaic structure, there is no sharp spatial cutoff from the slit. Without the adjustable slit, intensity cut off by the SiC tube but present in the unrestricted I_0 measurement overlaps significantly with the image plane, causing strongly distorted spectra where small capillary samples are barely visible. The slit opening is selected according to capillary diameter (0.8 mm) and position, ensuring only catalyst-filled capillary volume contributes to the spectrum.

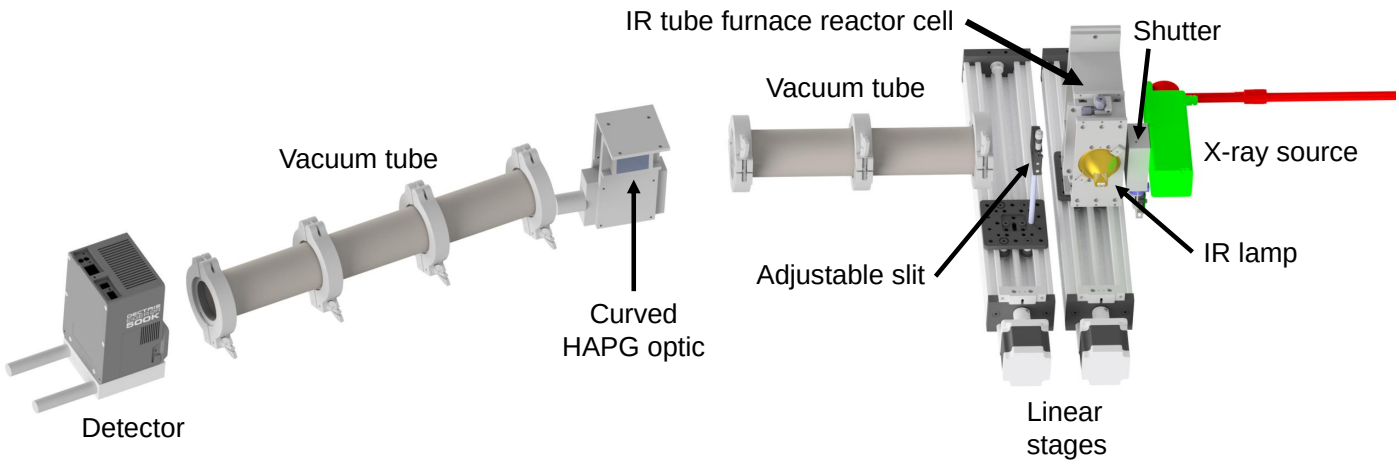

Fig. S1 CAD model of the modified von Hámos setup showing the IR tube furnace reactor cell orientation in the setup.

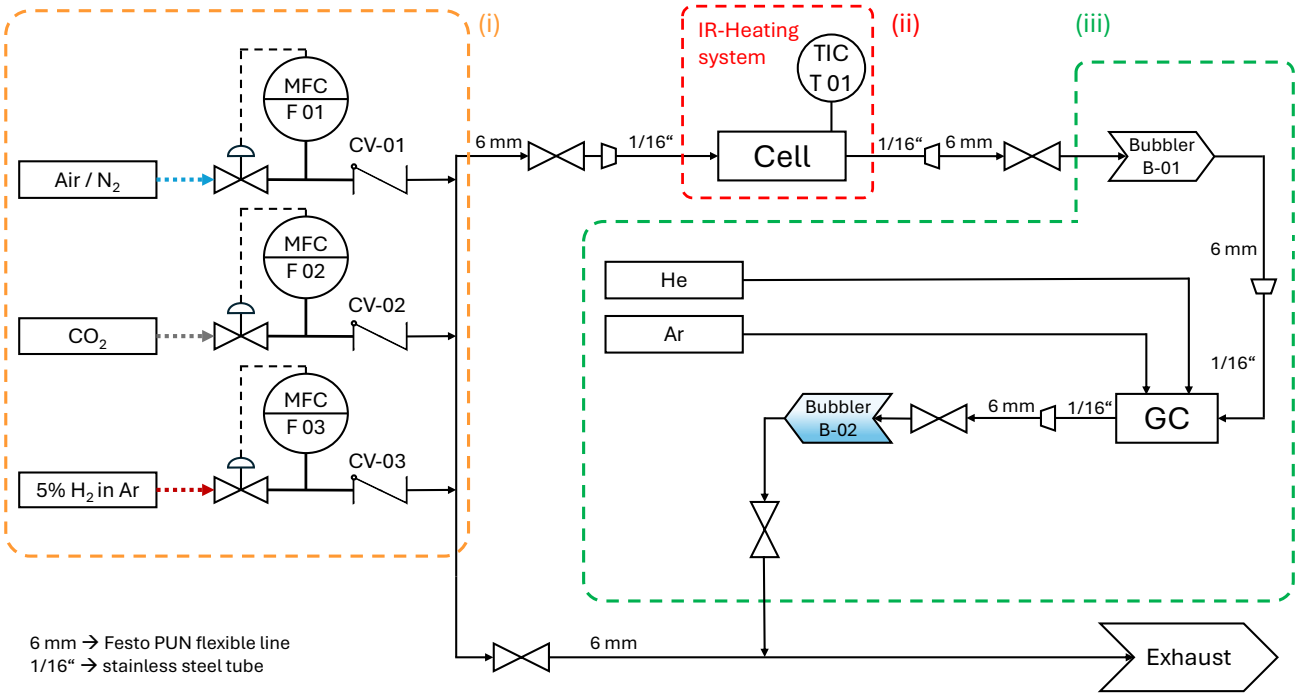

Fig. S2 P&ID of the *In situ/operando* reactor setup. With (i) gas flow control unit, (ii) reaction cell and (iii) gas analysis unit. MFC: mass flow controller; CV: check valve; TIC: temperature indicator and controller; GC: Gas chromatograph. Bubbler B-01 is empty to trap water during reaction. Bubbler-B02 contains water to indicate the gas flow. Optional: a pressure control unit (PC) can be installed between the reaction cell and Bubbler B-01.

1.2 IR-furnace reactor cell setup

The reactor cell design is based on Bischoff *et al.* [1] and was adapted for the laboratory von Hámos spectrometer (Fig. S3). A schematic of the full gas flow system (P&ID) is shown in Fig. S2. The setup comprises three main components: (i) upstream gas flow control, (ii) reaction cell, and (iii) downstream gas analysis (see subsections below). The cell can operate standalone or with gas flow/analysis as required.

(i) Upstream: Gas flow control

The upstream section (i) consists of three EL-Flow Prestige mass flow controllers (MFCs 01–03; Bronkhorst) connected to cylinders containing 5% H_2 in Ar (Arcal 15, Air Liquide),[7] CO_2 (Air Liquide),[8] and an in-house N_2/compressed air supply. Check-valves (CVs 01-03, Swagelok) prevent back-diffusion.

(ii) Reaction cell

Quartz capillaries (CM Scientific or Hilgenberg; 100±1 mm length) with 1.0/0.8 mm (OD/ID) dimensions were used for Mn/Ni K-edge measurements, providing low absorption and pressure tolerance ≥11 bar. Thicker 1.5/1.0 mm capillaries (≤50 bar, 1 000°C)[1] were tested for higher energies (Pt L-edge 11 564 eV,[9] Zr K-edge 17 998 eV[9]).

The capillary contains ∼5 mm catalyst bed flanked by 1 mm quartz wool plugs, with a Ø0.5 mm K-type thermocouple (Reckmann) positioned downstream in an isothermal region (Fig. 1a main text). Vertical orientation prevents sample displacement from gas flow/thermal expansion and ensures gas-sample contact before TC exposure. Mixed vespel/graphite ferrules (Mascom) with Swagelok T-pieces provide airtight sealing via quick-connect fittings.

A SiC tube with opposing 4×1 mm slits (Fig. S3) surrounds the capillary, serving as IR absorber while allowing X-ray transmission. SiC provides high hardness, IR absorption, and favorable X-ray transparency at elevated temperatures.[10,11] The complete assembly mounts on a transport plate (Fig. S3) for safe handling. Two 150 W IR halogen lamps (Osram 64635 HLX) heat the SiC tube (focal distance 19.5 mm), held by stainless steel brackets with anti-rotation screw.

Detailed cell performance data are provided by Bischoff *et al.* [1] Isolation valves enable standalone operation (Fig. S2).

(iii) Downstream: Gas analysis

The downstream section contains two bubblers (B-01, B-02) and GC unit for catalytic activity measurement (see Section 1.3). Bubbler B-01 traps moisture before GC; B-02 (water-filled) indicates gas flow.

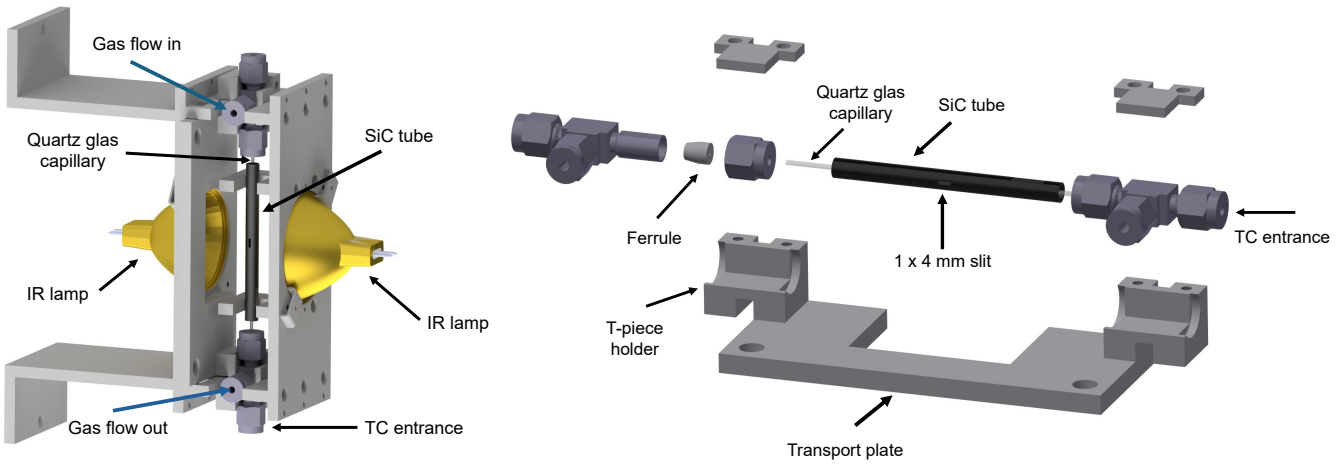

Fig. S3 Left: CAD model of the IR tube furnace reactor cell. Two IR lamps heat the SiC tube surrounding the loaded quartz capillary. Right: Exploded view of transport plate assembly. Vespel/graphite ferrules seal capillary to T-pieces; plate prevents movement during transport.

1.3 Gas chromatography

To measure the catalytic activity of the samples (in particular, CO_2 conversion as well as CH_4 and CO production) an online gas chromatograph (GC, Micro GC Fusion 2-Module system, INFICON GmbH, Cologne, Germany)[12] equipped with Rt-Molsieve 5 Å (in module A) and Rt-Q-Bond (in module B) columns, utilizing a thermal conductivity detector (TCD) was employed. Helium (He) and argon (Ar) gases were connected to the GC, each regulated to 4 bar pressure. Both gases served as reference gases for the two modules, ensuring accurate measurement of thermal conductivity differences between the sample and carrier gas in the TCD.

2 Sample systems and reaction context

In this work, two model systems were chosen to demonstrate the capabilities of the laboratory von Hámos–cell combination. First, a 5% Ni/MnO catalyst was used to follow Mn K-edge changes during the oxidation of MnO to Mn_2O_3 under *in situ* conditions. Second, a 20 wt% NiO/COK-12 (SiO_2) catalyst was employed as a representative Ni-based system for CO_2 methanation to study Ni K-edge changes during catalyst activation and under *operando* conditions.[1,13,14]

CO_2 methanation proceeds via:

$$CO_2 + 4H_2 \rightleftharpoons CH_4 + 2H_2O, \tag{1}$$

and competes with the reverse water-gas shift (RWGS) reaction,

$$CO_2 + H_2 \rightleftharpoons CO + H_2O. \tag{2}$$

At low pressures and high temperatures, CO is the thermodynamically preferred product, whereas CH_4 formation is favoured at higher pressures and moderate temperatures.[15] Ni catalysts are widely used for both reactions, and it is well established that NiO must be reduced to metallic Ni to become active in methanation, typically in the range 300–400 °C and 1–10 bar.[14] In this study, we use this well-known system to demonstrate that the cell enables tracking NiO reduction and the onset of catalytic activity via combined XAS and GC measurements.

2.1 5% Ni/MnO: synthesis and use as Mn model system

The 5% Ni/MnO catalyst used to investigate the *in situ* oxidation of MnO to Mn_2O_3 was synthesized as described by Gili *et al.*.[16,17] Specifically, it was prepared via a coprecipitation method using $Ni(OCOCH_3)_2 \cdot 4H_2O$ (nickel acetate tetrahydrate, Sigma-Aldrich) and $Mn(NO_3)_2 \cdot 4H_2O$ (manganese nitrate tetrahydrate, Sigma-Aldrich) as metal precursors, corresponding to a Ni:Mn atomic ratio of 0.05:0.95. The appropriate amounts of these precursors were dissolved in 100 mL of deionized (DI) water. To initiate coprecipitation, a second solution containing 55 mmol of $NaHCO_3$ (Merck) in 50 mL of water was added dropwise under vigorous stirring. The pH of this solution was adjusted to $\geq$10 using NaOH (Merck). After stirring for 8 h, the resulting precipitate was collected by filtration and washed several times with DI water. The solid was then dried under vacuum at 80 °C overnight, followed by calcination at 750 °C for 4 h with a heating rate of 5 °C min^{-1}.

After calcination of the synthesized catalyst, a part of the material was treated in a 5% H_2 in N_2 atmosphere at 500 °C for at least 60 min to reduce NiO/Mn_2O_3 to Ni/MnO. XRD measurements of the treated and untreated material confirm the successful reduction of Mn_2O_3 to MnO in the material (see Fig. S4).

2.2 20-NiO/COK-12: synthesis and use in CO_2 methanation

The synthesis of the COK-12 (ordered mesoporous SiO_2) support was performed in a batch upscaled by a factor of 50, as previously reported.[18] Briefly, 200 g of Pluronic P123 (MW 5800 g mol^{-1}, from Sigma-Aldrich, Merck, Germany) was dissolved in 5375 mL deionized water (DIW). To this solution, 168.1 g of anhydrous citric acid (≥99.5%, from Carl Roth GmbH+Co.KG, Karlsruhe, Germany), 144.1 g of trisodium citrate dihydrate (≥99%, from Carl Roth GmbH+Co.KG, Karlsruhe, Germany), and a solution of 520 g of sodium silicate (7.8–8.5 wt% Na_2O, 25.8–28.5 wt% SiO_2, from Carl Roth GmbH+Co.KG, Karlsruhe, Germany) in 1500 mL DIW were incorporated. After a day of aging at room temperature (RT), the precipitated solids were filtered from the aqueous solution, washed with 25 L DIW, and dried at 60 °C. The resulting powder was calcined at 500 °C for two hours to remove the organic template.

For metal loading, incipient wetness impregnation followed by vacuum drying was performed on the COK-12 support. 0.515 mL/$g_{COK\text{-}12}$ of a nickel nitrate hexahydrate aqueous solution ($Ni(NO_3)_2 \cdot 6H_2O$, from Merck, Darmstadt, Germany) (24.64 g $Ni(NO_3)_2 \cdot 6H_2O$ in 10 mL DIW) was added to 1 g of COK-12. The resulting light-green powder was vacuum-dried immediately after deposition using a vacuum furnace (VT 5042 EK, Heraeus, Germany) at RT for approximately 2 hours until dry. The powder was then placed in contact with a concentrated ammonia solution ($NH_3 \cdot H_2O$, 25%, from Carl Roth GmbH+Co.KG, Karlsruhe, Germany), causing a change of color to light blue due to the formation of the nickel-ammonia complex, after which it was vacuum-dried a second time. The obtained pre-catalyst, which contained approximately 20.2 wt% NiO (corresponding to 15.8 wt% Ni) after calcination as determined by quantitative X-ray fluorescence (XRF, see Section 4), is referred to as 20-NiO/COK-12 in this paper.

Prior to catalytic testing, the GC was calibrated to detect H_2, N_2, O_2, CO, and CH_4 in Module A, as well as CO_2 and C2–C4 hydrocarbons in Module B. Water could be qualitatively identified in Module B when required. During the catalytic experiments CH_4 was the only carbon-containing product detected, with overall carbon mass balances exceeding 93%. CO was below the detection limit of the GC. Flow compression effects were neglected due to the low conversion and minimal overall change in total mole number.

The reactions taken into account in the system are methanation and RWGS ((1)and (2)). The calculations for conversion, and selectivity were performed utilizing the dgbowl package.[19,20]

In summary, product- and carbon-based CO_2 conversion (X_{CO_2}), was calculated as:

$$X_{CO_2} = 100 \cdot \frac{[CO]_o + [CH_4]_o - [CO_2]_o}{[CO]_o + [CH_4]_o} \tag{3}$$

Where the subindex o refers outlet concentrations (calculated from GC data).

Selectivity towards methane (S_{CH_4}) was calculated as:

$$S_{CH_4} = 100 \cdot \frac{[CH_4]_o}{[CO]_o + [CH_4]_o} \tag{4}$$

2.3 Reference materials and additional samples

For the *in situ* Mn K-edge investigation of the 5% Ni/MnO catalyst, different manganese oxides (MnO, MnO_2 and Mn_2O_3) previously prepared on adhesive tape and used as references by Dimitrakopoulou *et al.*[21] were employed as reference standards.[21] In addition, the calcined catalyst (5% NiO/Mn_2O_3) and the reduced catalyst (5% Ni/MnO), which was measured *in situ*, were also prepared as pellets to assess artefacts introduced by the capillary and to allow direct comparison of the same material in different oxidation states. This is particularly important because the presence of Ni and the synthesis procedure (Section 2.1) may influence the Mn speciation and thus deviate from pure Mn oxide references.

For the *operando* Ni K-edge investigation of 20-NiO/COK-12, the catalyst itself was prepared as a pellet for *ex situ* measurements, together with NiO powder (Sigma-Aldrich) as an oxidic reference.[22] Pellet preparation followed the procedure described by Praetz and Schlesiger *et al.*[6] A 10 μm Ni foil (Goodfellow, 99.95%) was used as metallic Ni(0) reference.[23] Approximately 1 mg of 20-NiO/COK-12 was loaded into the capillary, which provided detectable catalytic activity under the chosen conditions while keeping the bed short enough to minimise temperature gradients along the irradiated region.[1]

To evaluate the performance of the combined *in situ/operando* setup and spectrometer across different energies and capillary types, additional samples were investigated. SnSe (tin selenide), a leading thermoelectric material,[24,25] was measured at the Se K-edge (12 658 eV)[9] to probe intermediate energies and capillary artefacts. The powder was obtained by gently crushing a Bridgman-grown single crystal (2D Semiconductors, BLK-SnSe) with a mortar and pestle.[26]

ZrO_2 (zirconium(IV) oxide, Alfa Aesar)[27] was measured at the Zr K-edge (17 998 eV)[9] using a 1.0 ± 0.1 mm inner and 1.5 ± 0.1 mm outer diameter capillary, as in Bischoff *et al.*[1] This sample was chosen to test the upper energy limit of the spectrometer. The material was diluted 1:2 with Hoechst Wax C to achieve an optimal absorption step for XAS.

3 XRD measurement of synthesized 5% Ni/MnO catalyst

Fig. S4 shows the diffraction pattern of the synthesized 5% Ni/MnO catalyst before (XXMD11_D1MD11, blue curve) and after (XXMD12_D1MD12, black curve) reduction with 5% H_2 in Ar at 500 °C for at least 60 min to reduce NiO/Mn_2O_3 to Ni/MnO.

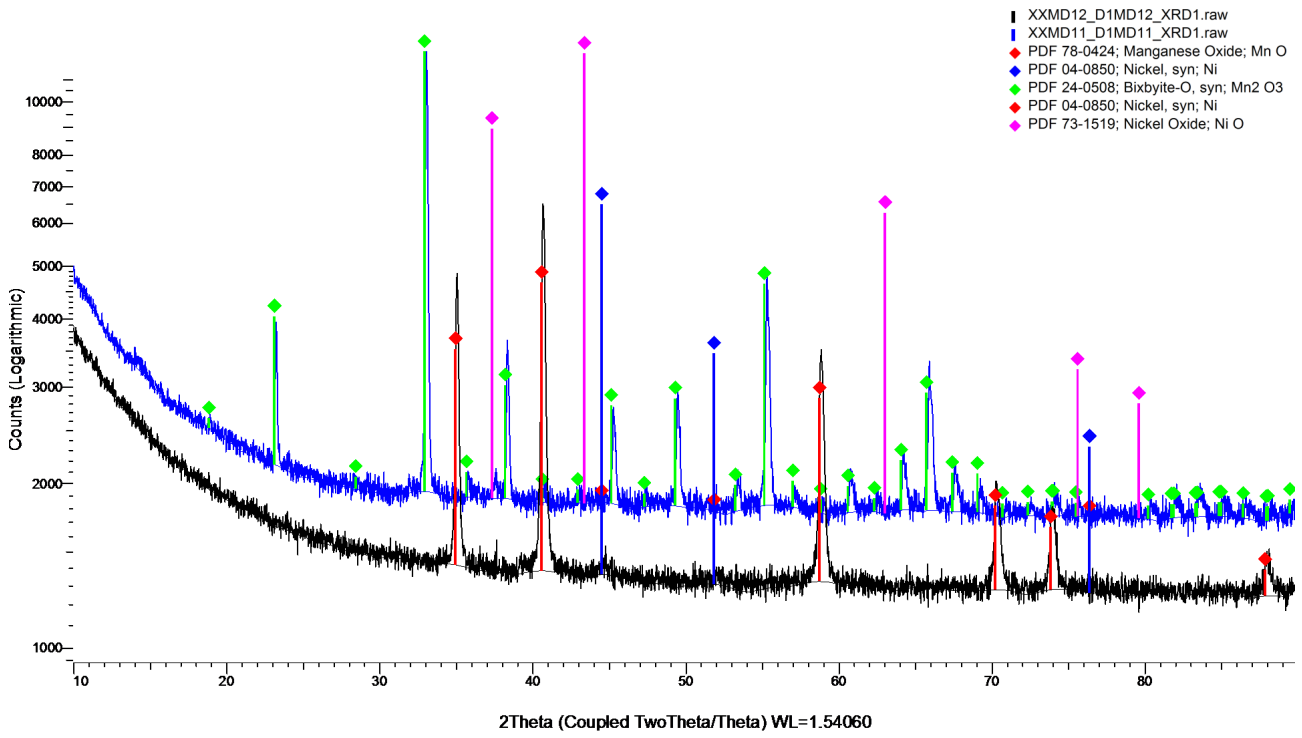

Fig. S4 XRD measurement of the synthesized 5% Ni/MnO catalyst before (XXMD11_D1MD11, blue curve) and after (XXMD12_D1MD12, black curve) reduction with 5% H_2 in Ar at 500 °C for at least 60 min to reduce NiO/Mn_2O_3 to Ni/MnO.

4 XRF measurements of 20-NiO/COK-12

Quantitative X-ray fluorescence (XRF) on the 20-NiO/COK-12 catalyst after calcination was performed using a *FISCHERSCOPE® X-RAY XDV®-SDD* spectrometer equipped with a microfocus tungsten X-ray tube and a beryllium window. Measurements were carried out at 50 kV without any primary filter. Component analysis revealed 20.2 wt% NiO and 79.8 wt% SiO_2, corresponding to approximately 15.8 wt% Ni content in the catalyst.

5 XAS normalization, artefacts and operando/in situ results

XAS spectra were normalized using the DEMETER/ATHENA software package.[28] Pre-edge subtraction was performed using a linear function fitted to the available pre-edge region, which was sufficiently defined even for spectra restricted to the XANES range. Post-edge normalization was carried out by fitting a polynomial function (second order) to the accessible post-edge region. In cases where the usable energy range was limited by a high-energy cut-off or exhibited curvature due to capillary-induced artefacts, the post-edge fit was restricted to the highest-energy region unaffected by the cuttoff. Identical normalization parameters and fitting ranges were applied consistently to all spectra within a given dataset, using common reference (isosbestic) points where applicable, ensuring reliable comparison of relative spectral changes during *operando* experiments.

5.1 Extended analysis: capillary artefacts and energy range performance

This section provides detailed analysis supporting Fig. 2 (main text), quantifying capillary-induced artefacts and spectrometer performance across its full energy range. K-edge XAS spectra of four reference systems (Mn 6 539 eV, Ni 8 333 eV, Se 12 658 eV, Zr 17 998 eV) [9] were recorded using appropriate capillary configurations. Unnormalized spectra (Fig. S5–S6) and normalized capillary vs pellet comparisons (Fig. S7, S8) systematically reveal energy-dependent limitations and capabilities.

Absorption and sample preparation effects: All samples were diluted to achieve $\mu Q \approx 1$ using boron nitride (BN) for heated *in situ/operando* experiments or Hoechst Wax C for room temperature measurements. The measured absorption step depends not only on analyte concentration and dilution ratio but also critically on capillary packing density, quartz wool compression effects, and dynamic changes during heated operation (thermal expansion, particle rearrangement). These factors necessitate individual normalization procedures for each measurement.

Mn K-edge (5% Ni/MnO, 1.0/0.8 mm capillary, 300 s acquisition): The spectrum is dominated by the XANES region with a sharp transmission cutoff at ∼6 650 eV, characteristic of the thin-wall capillary limit at low energies (Section 1.1). Despite modest SNR, this 5-minute acquisition proves sufficient to resolve oxidation state changes, as demonstrated in the full *in situ* Mn oxidation series (Section 5.2).

Ni K-edge (20-NiO/COK-12, 1.0/0.8 mm capillary, 300 s): Higher tube output and reduced capillary wall absorption significantly improve SNR compared to Mn, extending the usable post-edge range. However, the characteristic "round shape" distortion (dotted line, Fig. 2 main text) persists, arising from cylindrical geometry causing nonhomogeneous sampling across the spectrometer's energy bandpass. This meridional plane effect becomes the dominant limitation for operando studies.

Se K-edge (SnSe, 1.0/0.8 mm capillary, 300 s): Geometric distortions are markedly reduced. At intermediate energies, thicker 1.5/1.0 mm capillaries become practical, achieving sufficient SNR within 5–15 minutes – particularly valuable for high-pressure (11–50 bar) operation where thin capillaries would fail.

Zr K-edge (ZrO_2+Hoechst Wax C, 1.5/1.0 mm capillary, 120 s): Negligible geometric distortion and no observable transmission cutoff. High SNR XANES with clear edge jump and white line features confirms that thick-wall capillaries provide excellent performance at the spectrometer's upper energy limit, enabling *in situ/operando* studies up to 50 bar with minimal artefacts.

These systematic measurements establish clear operational guidelines: thin capillaries (1.0/0.8 mm) remain mandatory below 10 keV despite artefacts, while thick-wall capillaries (1.5/1.0 mm) become the method of choice above 12 keV for high-pressure applications.

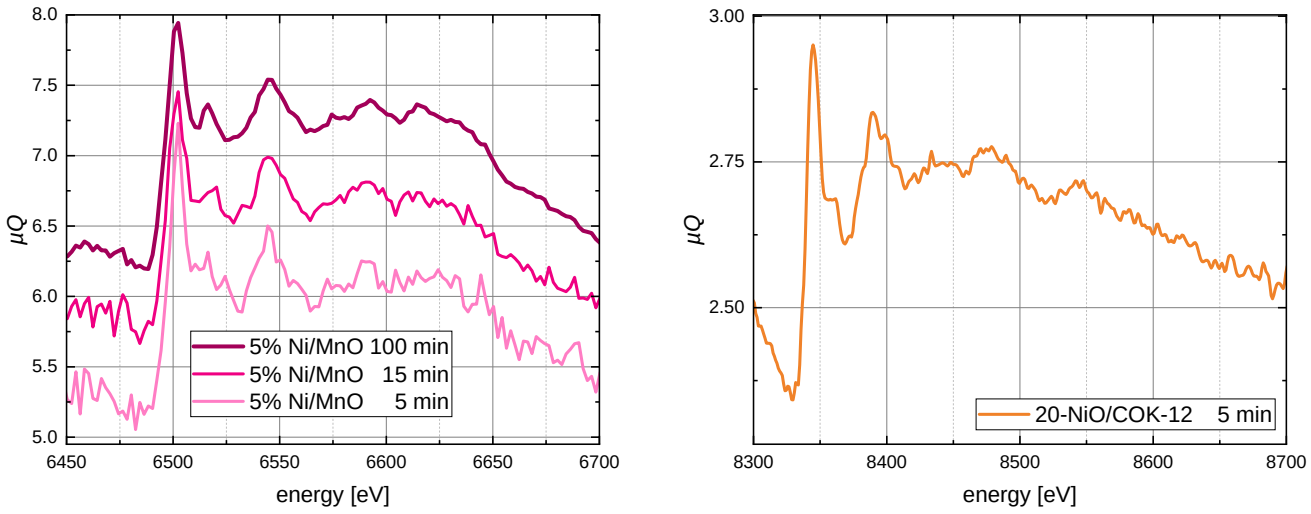

Fig. S5 Left: Mn K-edge XAFS spectrum of 5% Ni/MnO_2 measured in a 1.0/0.8-capillary at RT for different measurement times. Right:Ni K-edge XAFS spectrum of 20-NiO/COK-12 measured in a 1.0/0.8-capillary at RT. The measurement time was 5 min (300 s).

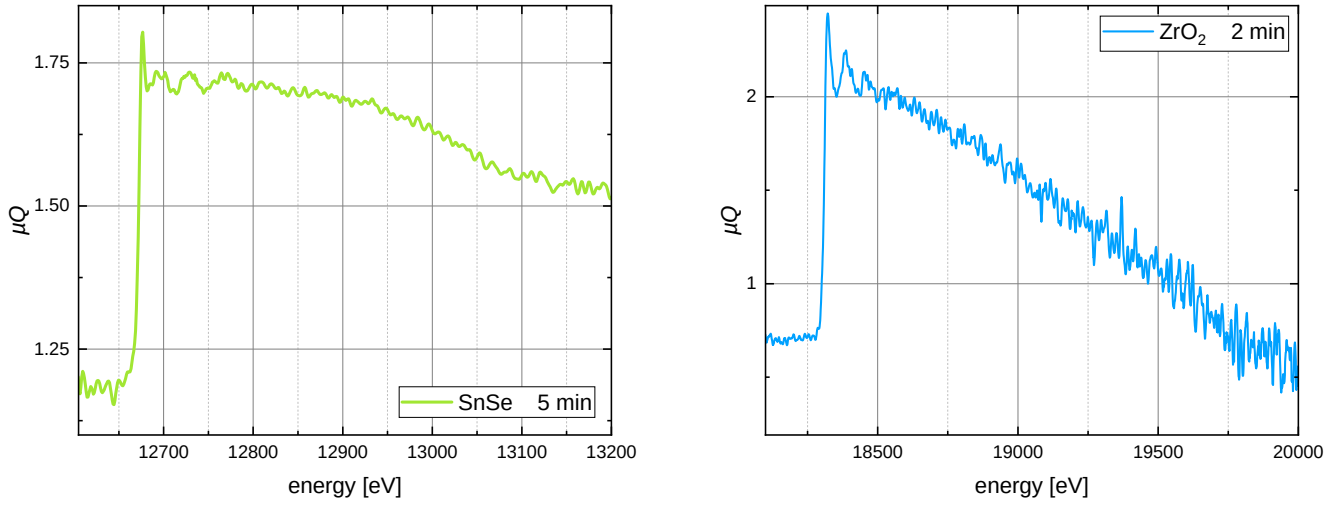

Fig. S6 Left: Se K-edge XAFS spectrum of SnSe measured in a 1.0/0.8-capillary at RT. The measurement time was 5 min (300 s). Right:Zr K-edge XAFS spectrum of ZrO_2 measured in a 1.5/1.0-capillary at RT. The measurement time was 2 min (120 s).

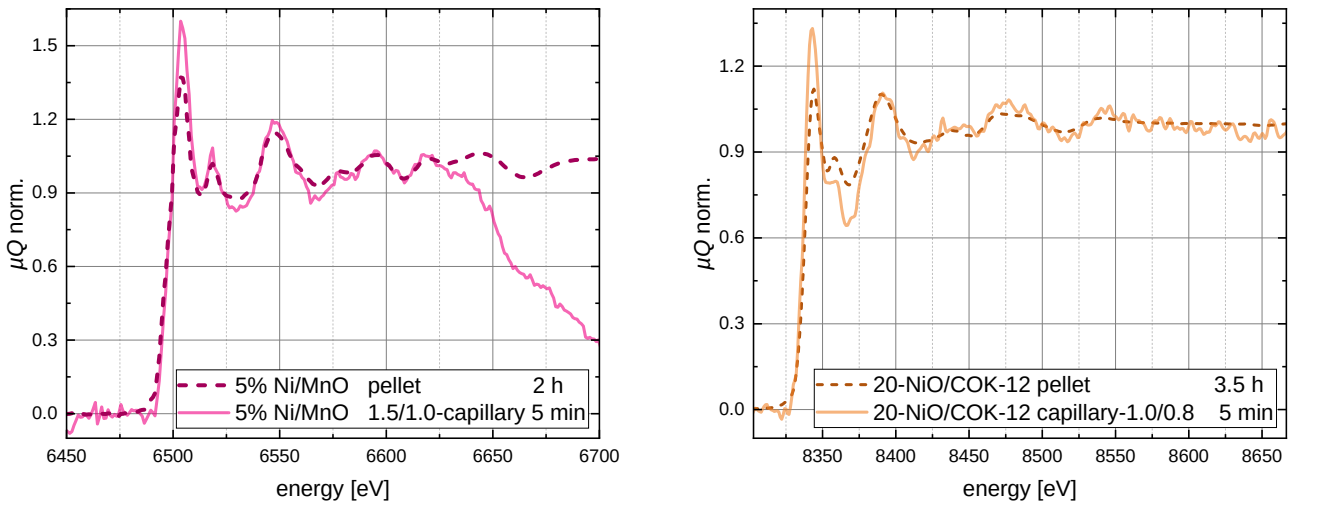

Fig. S7 Normalized Mn K-egde XAFS spectra of 5% Ni/MnO_2 in a 1.0/0.8-capillary in comparison to a pellet sample of the same material (left) and Ni K-edge spectra of 20-NiO/COK-12 in a 1.0/0.8-capillary in comparison to pellet sample of the same material (right).

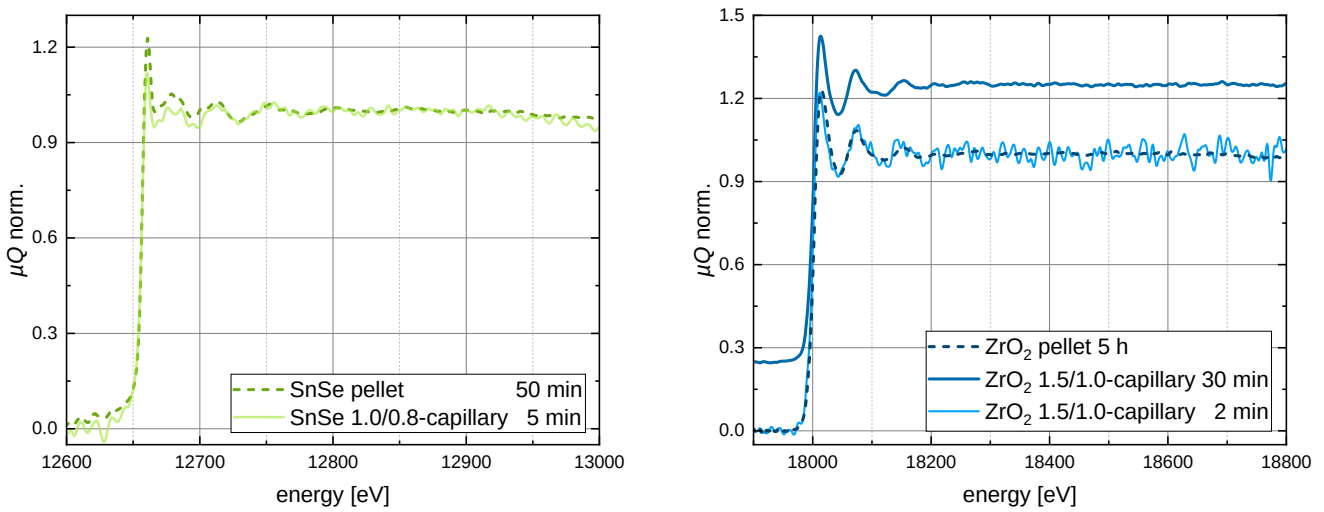

Fig. S8 Normalized Se K-egde XAFS spectra of SnSe in a 1.0/0.8-capillary in comparison to a pellet sample of the same material (left) and Zr K-edge spectra of ZrO_2 in a 1.5/1.0-capillary in comparison to pellet sample of the same material (right).

5.2 *In situ* Mn K-edge oxidation: 5% Ni/MnO

This section presents an additional measurement demonstrating the capability to track oxidation state changes in a second sample system at lower energies (Mn K-edge). The reduced 5% Ni/MnO catalyst (BN diluted 1:8) was heated stepwise from RT to 600°C in compressed air (3 mL/min NTP) with 15 min spectra (300 s × 3 binning) at each temperature step. Results are compared to *ex situ* pellet references of reduced (Ni/MnO) and oxidized (NiO/Mn_2O_3) material.

Significant spectral evolution begins at 400 °C, with edge shift toward higher energies and white line intensity changes characteristic of $MnO \rightarrow Mn_2O_3$ oxidation (Fig. S9b). Oxidation completes 15 min after reaching 600 °C. Low flow rates resulted from partial capillary clogging by packed BN-diluted powder. Repeated measurements with different dilutions confirmed reproducibility.

Quantitative analysis via linear combination fitting (LCF) used ATHENA[28] with Ni/MnO and NiO/Mn_2O_3 pellet references over a fitting range from 20 eV before and 125 eV beyond the egde. LCF fractions represent spectral contributions (not weight/atomic %; see Note below). Results show initial oxidation at 200 °C (7% Mn_2O_3), accelerating to 47±4% at 400 °C and 97±5% at 600 °C (Fig. S13). Full LCF spectra (Fig. S10–S12) and fit statistics (Table S1) confirm excellent agreement.

Note: LCF fractions reflect spectral similarity to references. Bulk composition requires combining LCF results with known oxide content and molar masses.

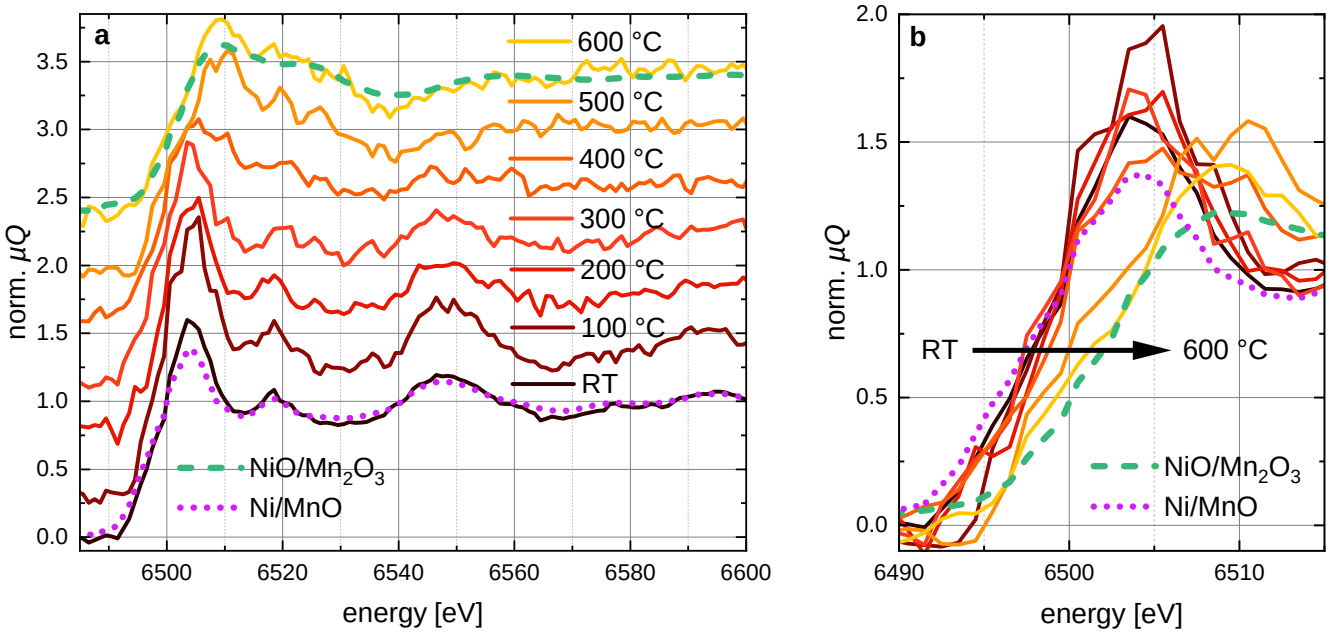

Fig. S9 *In situ* Mn K-edge XAS of 5% Ni/MnO during stepwise heating in air (15 min/spectrum). a: XANES evolution with Ni/MnO (reduced) and NiO/Mn_2O_3 (oxidized) pellet references. b: Edge shift highlighting Mn(II)→Mn(III) oxidation. Offset applied for clarity.

5.2.1 LCF details

LCF results at all temperatures (20 eV pre-/125 eV post-edge) are shown in Fig. S10–S12. The 100 °C spectrum matches RT within fit uncertainty. Fit statistics (R-factor, χ^2, χ^2_ν) in Table S1 confirm quality.

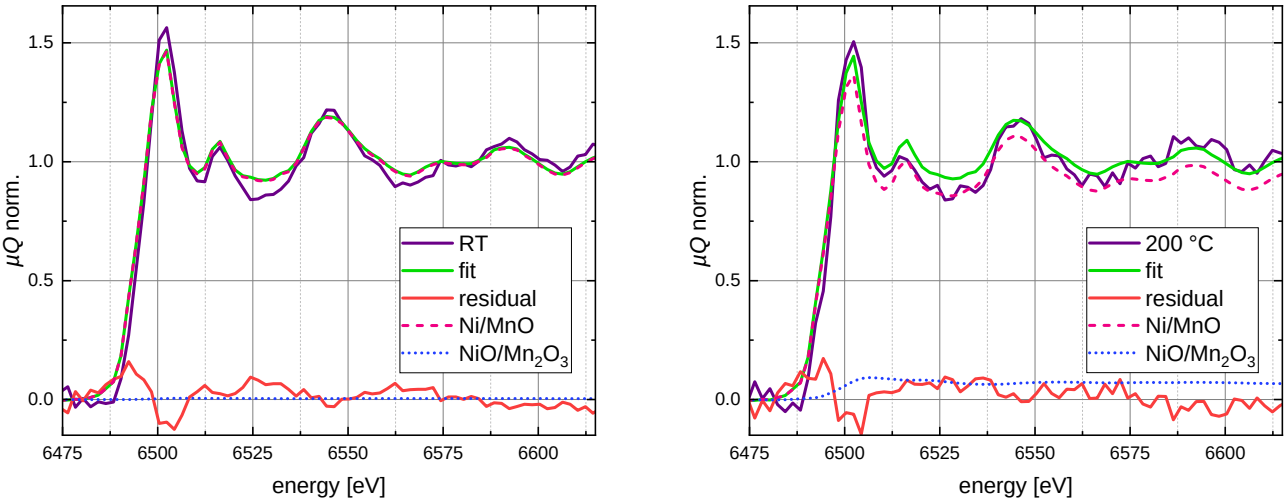

Fig. S10 Linear combination fitting (LCF) of the *in situ* Ni/MnO Mn K-edge XAS measurement at RT (left) before heating and at 200 °C (right).

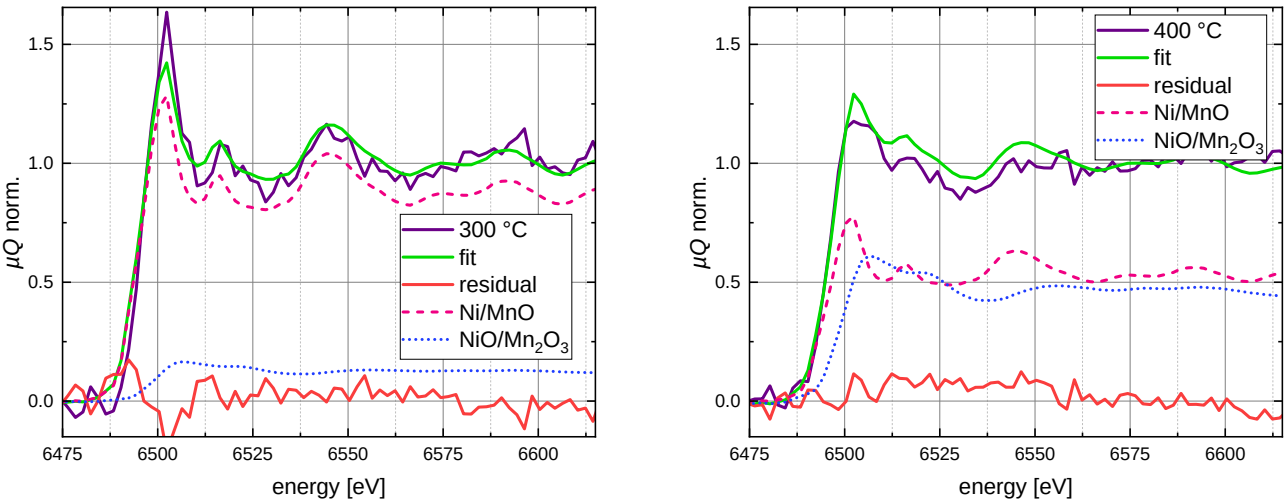

Fig. S11 Linear combination fitting (LCF) of the *in situ* Ni/MnO Mn K-edge XAS measurement at 300 °C (left) and at 400 °C (right).

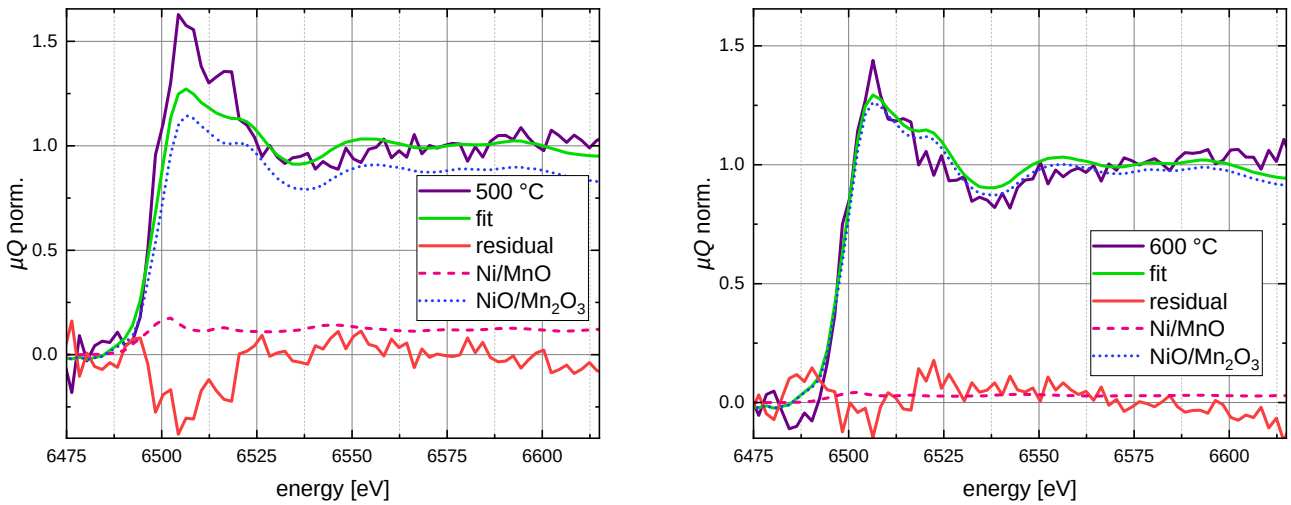

Fig. S12 Linear combination fitting (LCF) of the *in situ* Ni/MnO Mn K-edge XAS measurement at 500 °C (left) and at 600 °C (right).

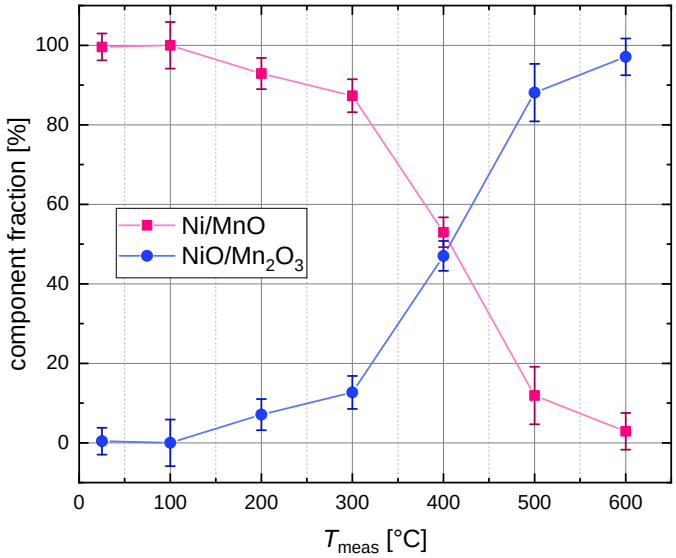

Fig. S13 Component fraction during *in situ* oxidation derived from the LCF (Fig. S10–S12). The references used for the LCF are Ni/MnO and NiO/Mn_2O_3.

Table S1 LCF results at different temperatures T using Ni/MnO and NiO/Mn_2O_3 as standards. Uncertainties are given as ± values. Reduced chi-square (χ^2_ν) and raw chi-square (χ^2) values are reported to assess the fit quality, with χ^2_ν accounting for the degrees of freedom.

T [°C]	R-factor	χ^2_ν	χ^2	Ni/MnO	NiO/Mn_2O_3
25	0.0222	0.00256	0.18691	1.00 ± 0.04	0.00 ± 0.04
100	0.0579	0.00769	0.56133	1.00 ± 0.06	0.00 ± 0.06
200	0.0306	0.00346	0.25221	0.93 ± 0.04	0.07 ± 0.04
300	0.0330	0.00385	0.28113	0.87 ± 0.05	0.13 ± 0.05
400	0.0337	0.00315	0.22986	0.53 ± 0.04	0.47 ± 0.04
500	0.0886	0.01167	0.85190	0.12 ± 0.08	0.88 ± 0.08
600	0.0373	0.00477	0.34836	0.03 ± 0.05	0.97 ± 0.05

5.3 Complete *operando* Ni K-edge dataset: 20-NiO/COK-12

This section presents the full *operando* dataset supporting the main text analysis (Fig. 2), covering all three experimental stages of the calcined 20-NiO/COK-12 catalyst: (1) initial CO_2:H_2 (nominal 4:1, 19.2 mL/min 5% H_2/Ar + 0.6 mL/min CO_2 at NTP) testing at 350 °C, (2) reduction/activation in 5% H_2/Ar (14.6 mL/min NTP) at 600 °C, and (3) post-reduction methanation testing at 350°C. Spectra were acquired every 300 s (5 min) with 1 °C/s ramps. Undiluted catalyst (∼1 mg) was loaded into 1.0/0.8 mm capillaries. LCF analysis used 20-NiO/COK-12 pellet and Ni foil references over range 20 eV pre-/250 eV post-edge.

Gas flow note: CO_2 MFC operated near lower limit (actual ∼0.23 mL/min vs nominal 0.6 mL/min); effective H_2:CO_2 ≈4:1 confirmed by GC. All flows reported are nominal. WHSV = 1.2×10^6 mL/(h · g_{cat}).

5.3.1 Complete time-resolved dataset

Fig. S14 presents synchronized LCF component fractions (a-c), GC analysis (d-f), and temperature/flow profiles (g-i) versus concatenated time-on-stream (TOS). Dashed lines mark transitions between stages.

5.3.2 Stage 1: Pre-reduction methanation (350 °C, 1 h)

Normalized spectra (Fig. S15a) show no evolution, consistent with inactive NiO state. GC confirms no CH_4/CO formation (Fig. S14d). Capillary vs. pellet reference differences are evident: white line intensity variations and lower edge step (0.5 vs 1.3) result from cylindrical geometry artefacts (Section 5.1) and challenging normalization of distorted spectra. Pellet damping may arise from pinhole effects; high absorption steps cause XANES damping.[29] Raw data covering flow introduction, RT→ 350 °C heating, and cooling (Fig. S20) show

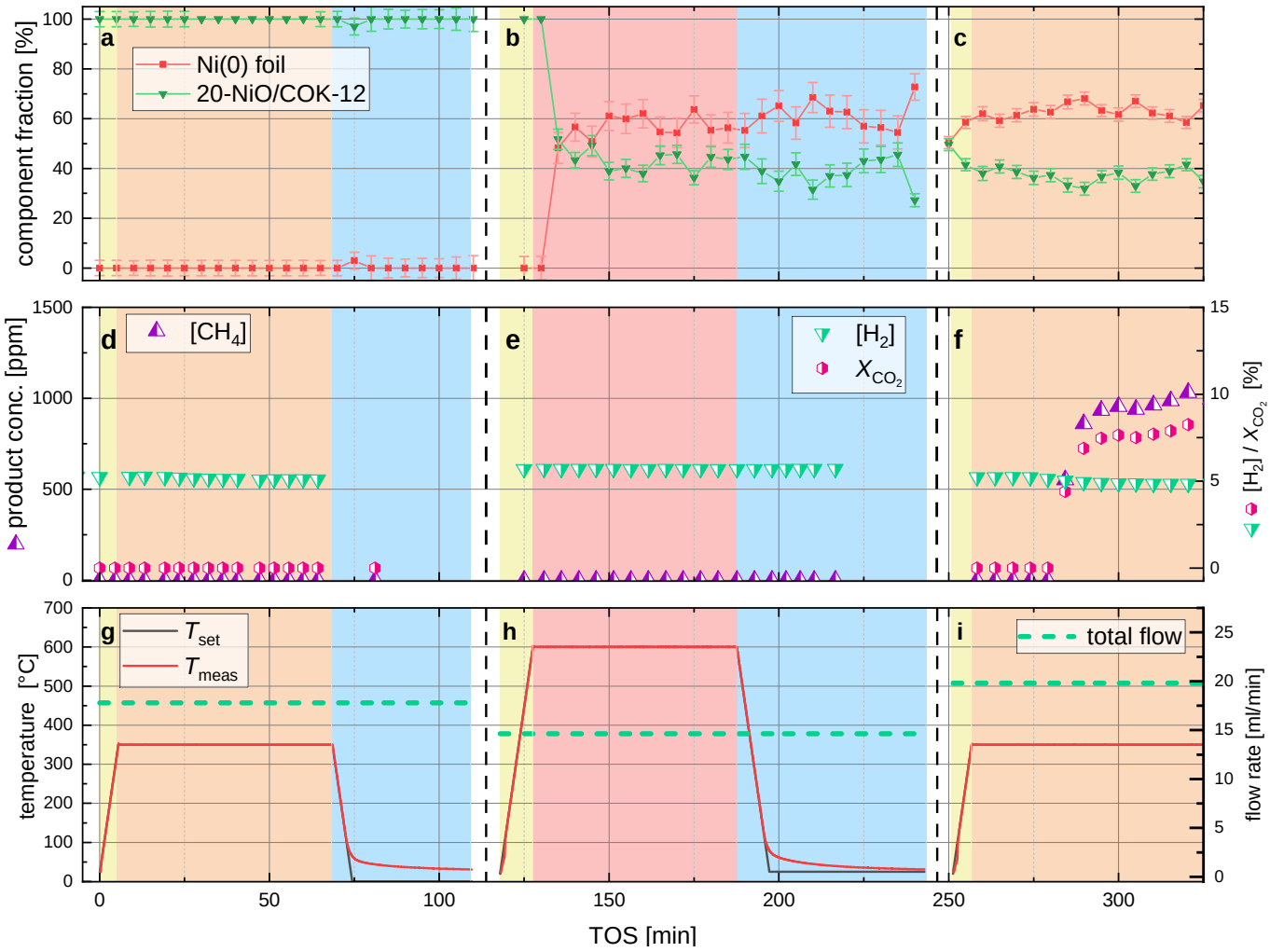

Fig. S14 Complete *operando* time evolution of 20-NiO/COK-12. Top row (a–c): LCF-derived Ni(0) component fractions from Ni K-edge XAS. Middle row (d–f): GC analysis showing [H_2], [CO_2], [CH_4] concentrations and CO_2 conversion (X_{CO_2}). Bottom row (g–i): temperature profile and total gas flow rate. Data plotted versus concatenated time-on-stream (TOS) with dashed lines marking transitions between experimental stages: pre-reduction methanation at 350 °C (a,d,g), H_2 reduction/activation at 600 °C (b,e,h), and post-reduction methanation at 350 °C (c,f,i) with WHSV = 1.2×10^6 mL/(h · g_{cat}). Note that TOS does not represent chronological elapsed time but cumulative experimental stages.

H_2 flow-induced packing density increase (∼10% mass loading) stabilizing after 10-15 min, with no spectral feature changes during thermal cycling.

5.3.3 Stage 2: Reduction/activation (600 °C, 65 min total)

Central result (main text Fig. 2(a-b)): Spectral evolution during 5 % H_2/Ar reduction (Fig. S15b) shows edge shift toward Ni(0) and white line intensity decrease above ∼450–500 °C. Reduction onset occurs at 471(85) °C (2nd spectrum during ramp, Fig. S14b). After 15 min at 600.0(1) °C hold, edge position matches Ni foil reference; ∼20 min hold yields majority Ni(0) phase. No H_2 consumption detectable due to low catalyst loading.

During cooling, EXAFS oscillations (8400 eV to 8600 eV) become more pronounced as Debye-Waller damping decreases. Post-cooling LCF robustness analysis (XANES, EXAFS, full spectrum) gives consistent 55–74% Ni(0) for 2nd-to-last 5-min spectrum; 50-min RT measurement yields 62–74% Ni(0) (see Fig. S16). The 50-min RT spectrum shows strong EXAFS agreement with Ni foil but XANES differences indicating incomplete reduction (residual Ni^{2+}). This is consistent with core-shell Ni/NiO morphology and metal-support interactions (MSI) with the COK-12 silica matrix.[30]

These MSI effects also explain pre-reduction discrepancies: 20-NiO/COK-12 exhibits higher edge position vs. pure NiO (Table S2) and EXAFS deviations (Fig. S17). Silica stabilizes Ni nanoparticles, potentially forming Ni-silicates.[31–33]

Raw data sequence (Fig. S21): Flow introduction at RT causes packing density increase (∼10% mass loading after 10–15 min stabilization); RT→600 °C ramp and hold captures complete reduction evolution; cooling to RT shows structural sharpening; pre/post-reduction comparison confirms incomplete reduction with residual Ni^{2+} contributions.

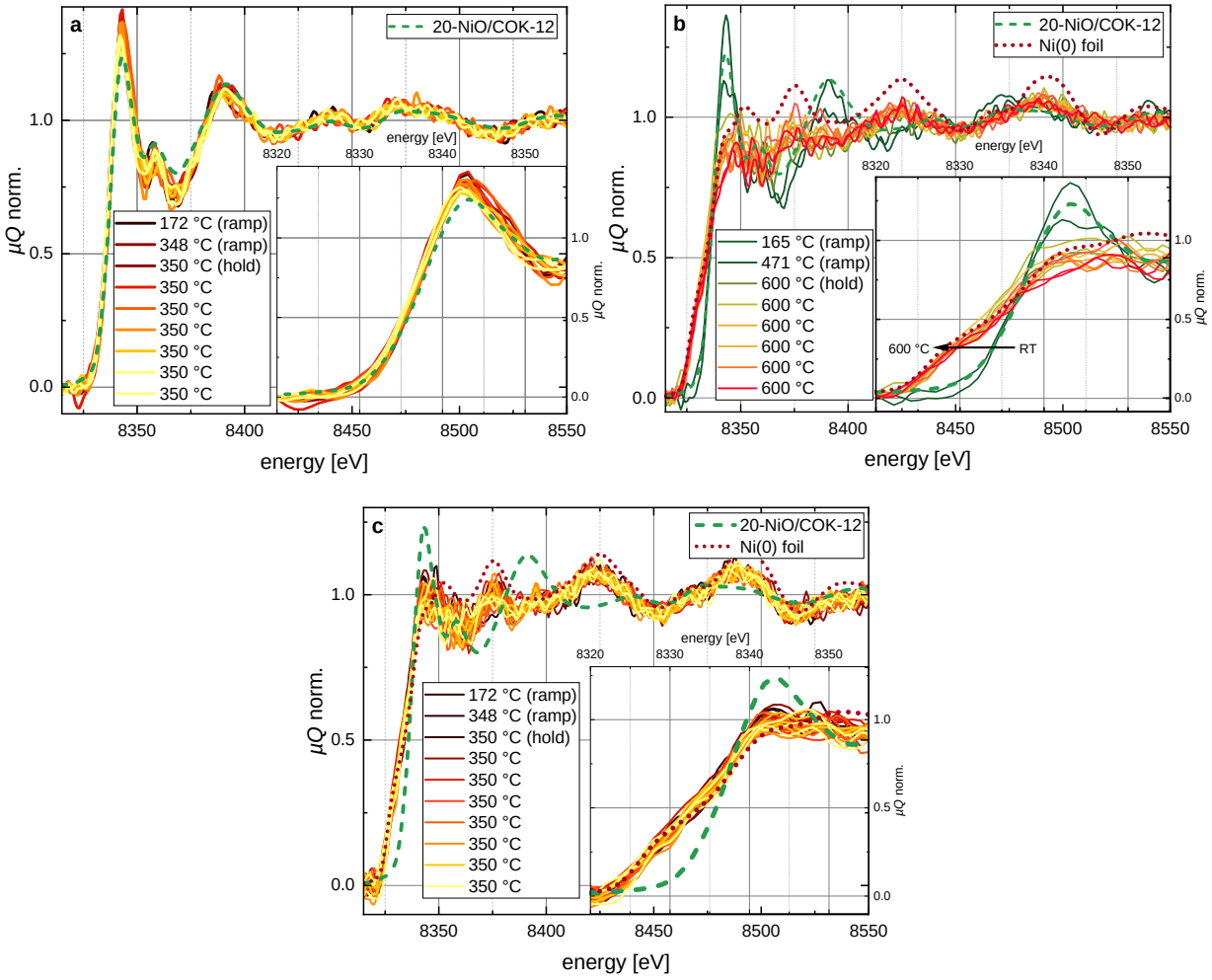

Fig. S15 *Operando* XAS measurements of 20-NiO/COK-12 at the Ni K-edge. a: Before catalyst activation, measured at 350 °C for 1 h under H_2/CO_2 flow at a 4:1 ratio. b: Catalyst reduction/activation at 600 °C for 1 h under pure H_2 flow. c: After activation, measured again at 350 °C for 2 h under the same H_2/CO_2 (4:1) conditions as the initial state. Each spectrum was acquired with a measurement time of 300 s (5 min). The results are shown alongside the reference spectra of 20-Ni0/COK-12 prepared as pellet and a 10 μm Ni(0) metal foil with a total acquisition time of 3.5 h and 1.5 h, respectively.

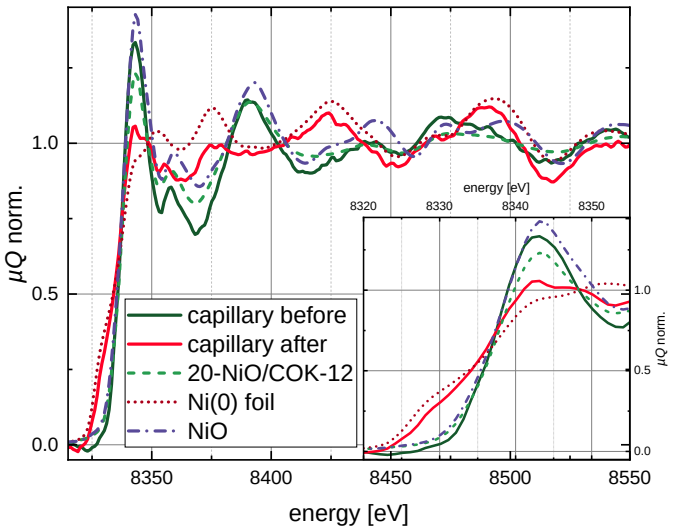

Fig. S16 Normalized XAS measurement of 20-NiO/COK-12 before and after reduction/activation procedure, with 50 min measurement time in comparison to 20-NiO/COK-12 prepared as free standing pellet, NiO and a 10 µm Ni foil. [23]

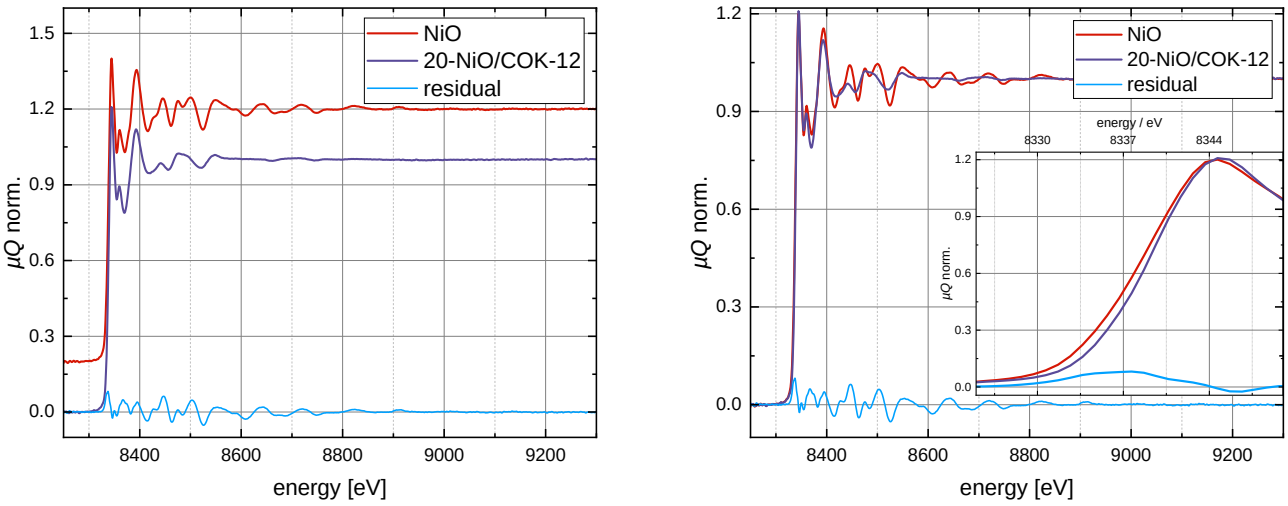

Fig. S17 Normalized XAS spectra of the reference sample NiO and 20-NiO/COK-12 before reduction, both samples prepared as pellets. Left: shows both spectra with an offset. Right: direct comparison, including an inset with the edge region showing a slight shift of 20-NiO/COK-12 towards higher energies.

Table S2 Comparison of Ni K-edge positions of the measured references and 20-NiO/COK-12 determined using the half-step and first maximum of the first derivative methods.

Sample	Half-step [eV]	Second derivative [eV]
Ni foil	8337.48 ± 0.03	8327.21 ± 0.08
NiO	8336.95 ± 0.04	8339.22 ± 0.14
20-NiO/COK-12	8337.71 ± 0.04	8338.56 ± 0.21

5.3.4 Stage 3: Post-reduction methanation (350 °C, 2 h + validation)

Immediate CH_4 formation ($\sim$1 000 ppm, $X_{CO_2} \approx 10(4)$ %, 100% selectivity, Fig. S14f) confirms catalytic activation of reduced Ni phase. No significant spectral evolution expected or observed (Fig. S15c); minor variations reflect Debye-Waller effects and gas evolution-induced particle motion. Flow doubling at $\sim$5 000 s (83 min) TOS – in the cumulative time axis in Fig. S25 at $\sim$333 min – dilutes CH_4 signal; 400 °C operation under doubled flow enhances activity (expected temperature effect) without structural changes. Lower conversions vs. literature reflect high WHSV and dilute feed.[14]

Raw data sequence (Fig. S22): Flow re-introduction at RT causes packing stabilization; RT $\rightarrow$ 350 °C heating shows no phase change; 350 $\rightarrow$ 400 °C validation confirms stable Ni(0) phase with increased CH_4 production; cooling from 400 °C shows reversible Debye-Waller broadening.

5.3.5 LCF methodology and validation

Primary LCF results (Fig. S14a-c) used full -20/+250 eV range. Robustness validated across XANES (-20/+50 eV), EXAFS (+50/+250 eV), and complete ranges. Final 600 °C spectrum LCF and time-resolved fractions shown in Fig. S18, S19.

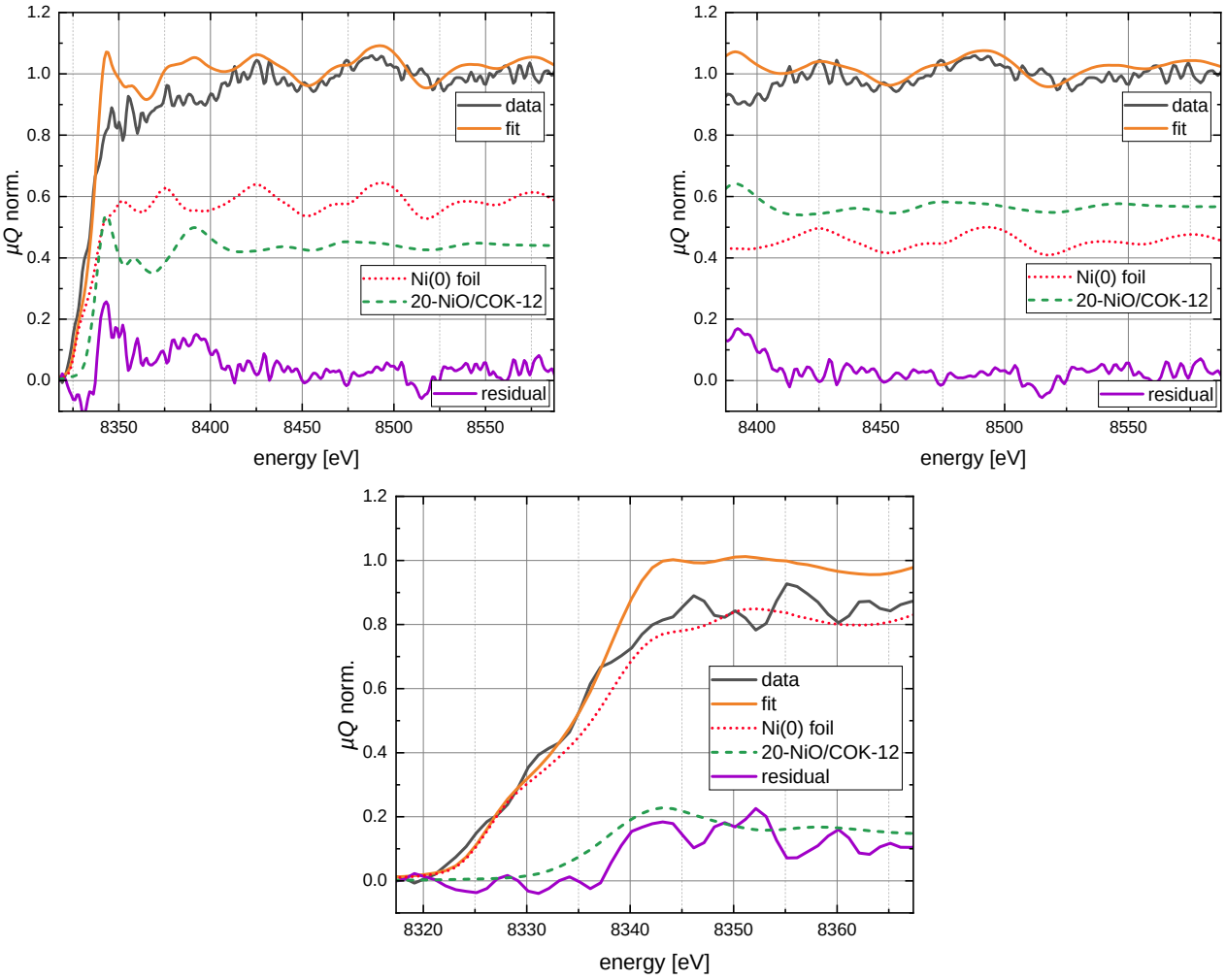

Fig. S18 LCF of the last *operando* spectrum at 600 °C alongside the fitted component fraction and the residual of fit and data for the three different fitting ranges. Top left: wide range covering 20 eV before to 250 eV beyond the edge. Top right: mid range covering 50 eV to 250 eV beyond the edge. Bottom: narrow edge covering 20 eV before to 30 eV beyond the edge.

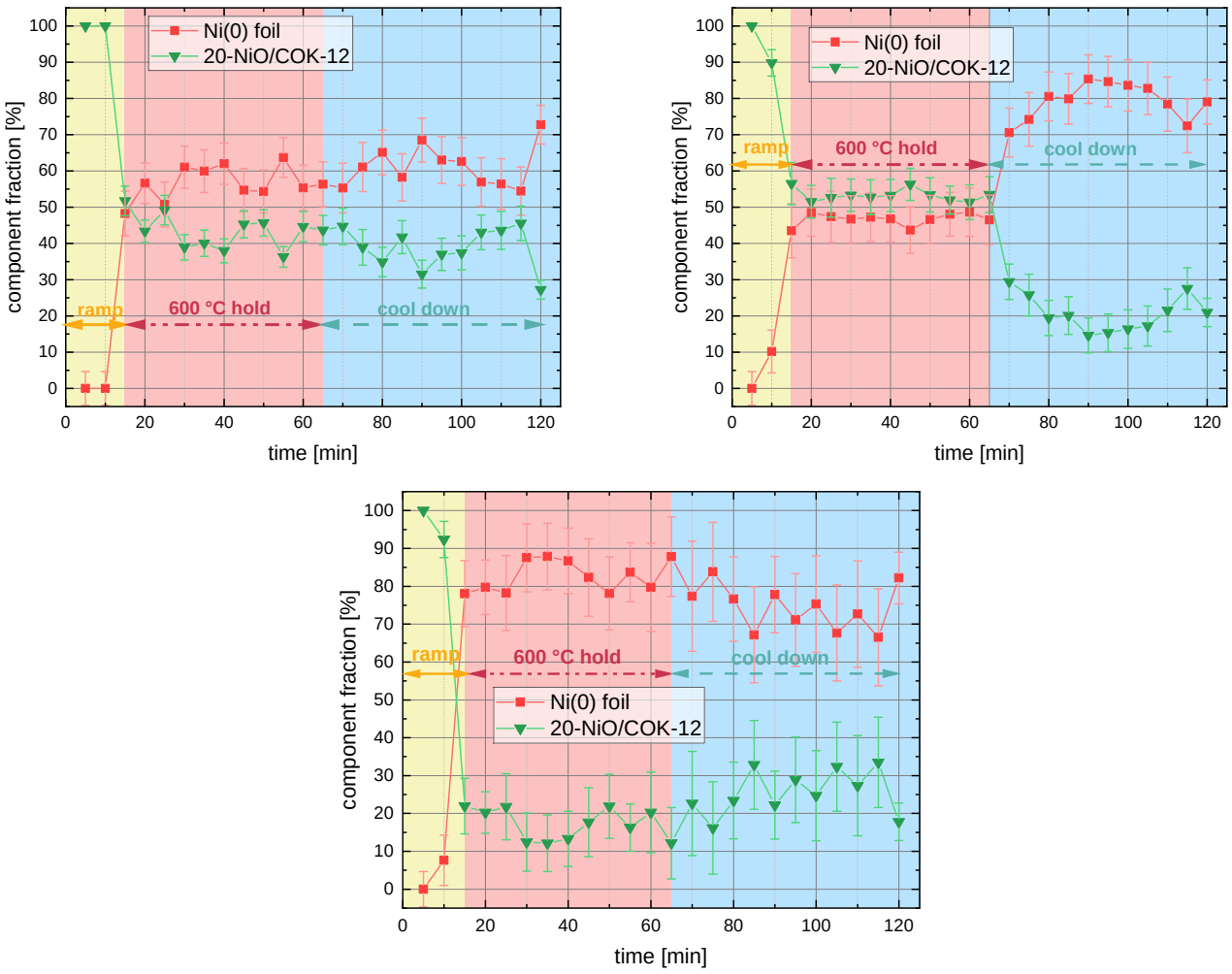

Fig. S19 Fractional component of the LCF of the complete reduction measurement from starting heating (ramp) to cool down, after holding the temperature 600 °C for 55 minutes, for the three different fitting ranges. Top left: wide range covering 20 eV before to 250 eV beyond the edge. Top right: mid range covering 50 eV to 250 eV beyond the edge. Bottom: narrow edge covering 20 eV before to 30 eV beyond the edge.

5.3.6 Raw/unnormalized *operando* measurements of 20-NiO/COK-12

The raw *operando* XAS measurements of 20-NiO/COK-12 are shown in Fig.S20 (before activation), Fig.S21 (during activation/reduction), and Fig.S22 (after activation).

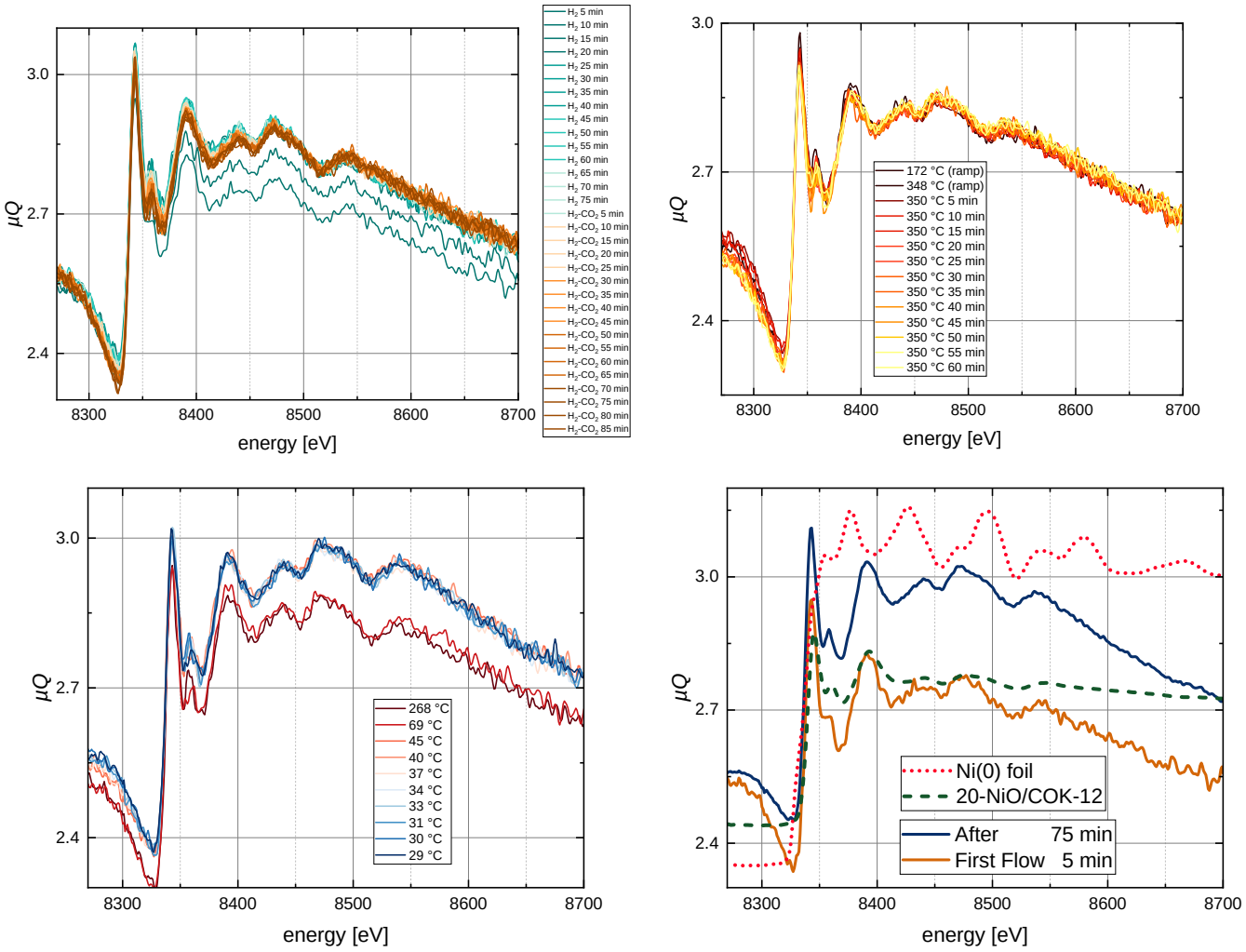

Fig. S20 Raw *operando* XAS spectra under reaction condition, with H_2 (17.2 mL/min 5% H_2/Ar at NTP)) and CO_2 (0.6 mL/min CO_2 at NTP)) gas flow in the ratio of 4:1 at 350 °C, before activation of the catalyst. Top left: during gas flow setup at RT. Top right: during heating from RT to 350 °C. Bottom left: during cool down to RT. Bottom right: comparison of first spectrum during flow and long measurement after the operando measurement alongside the reference spectra of a Ni metal-foil and the material 20-NiO/COK-12 prepared as pellet.

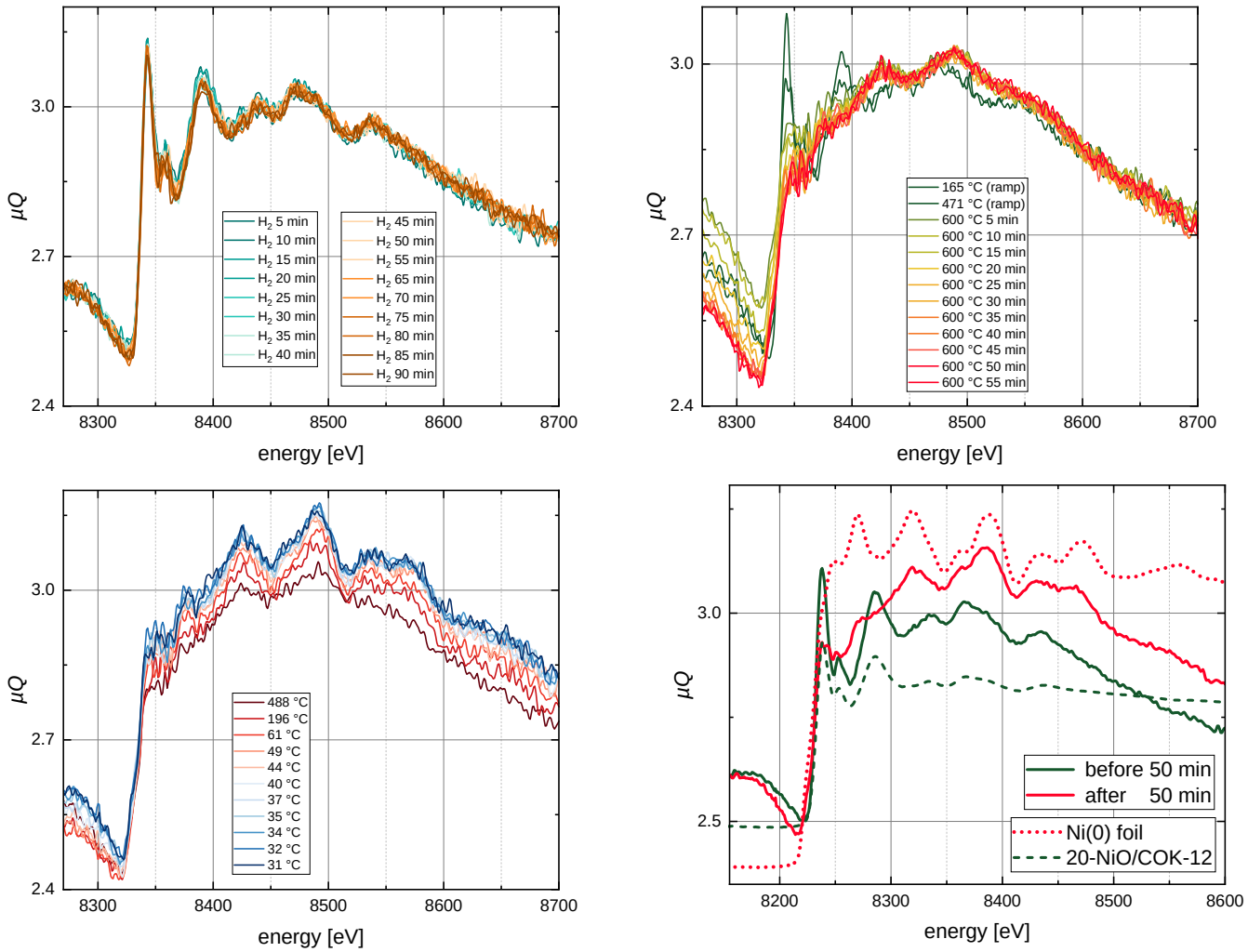

Fig. S21 Raw *operando* XAS spectra during the reduction/activation of the catalyst. Top left: during gas flow setup at RT. Top right: during heating from RT to 600 °C. Bottom left: during cool down to RT. Bottom right: Comparison before and after reduction with H_2 flow at 600 °C.

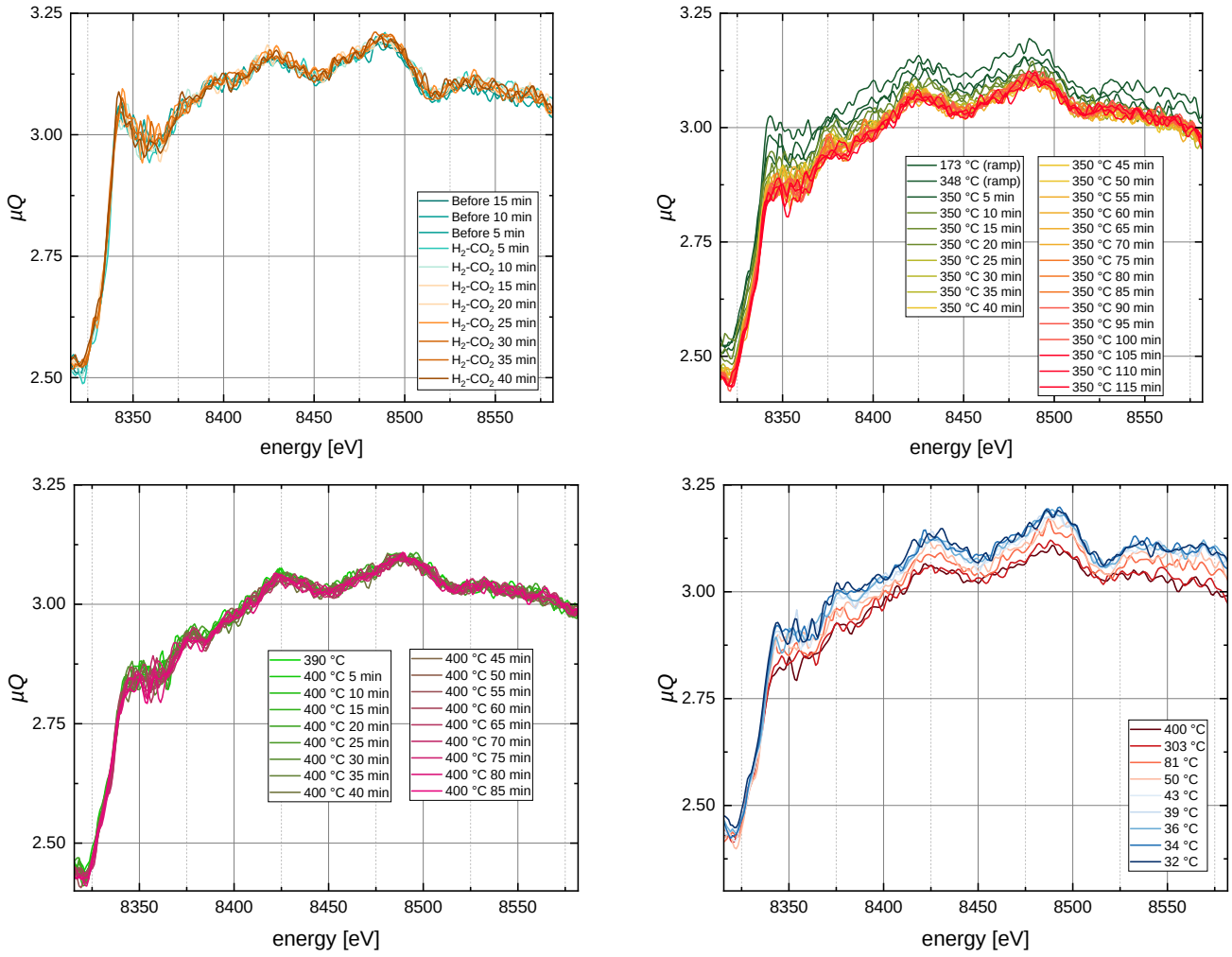

Fig. S22 Raw *operando* XAS spectra under reaction condition, with H_2 and CO_2 gas flow in the ratio of 4:1 at 350 °C, after reduction/activation of the catalyst. Top left: during gas flow setup at RT. Top right: during heating from RT to 350 °C. Bottom left: further increasing the temperature from 350 °C to 400 °C. Bottom right: during cool down from 400 °C to RT.

6 GC measurements

This section presents the measurements obtained using the online gas chromatograph (Micro GC Fusion 2-Module System, INFICON GmbH, Cologne, Germany). Fig. S23 displays the chromatograms from Module A (left, Rt-Molsieve 5 Å) and Module B (right, Rt-Q-Bond) recorded during operation of the 20-NiO/COK-12 catalyst at 400 °C under a H_2/CO_2 flow, after activation.

Fig. S24 provides a direct comparison of the catalyst measured at 350 °C under a H_2/CO_2 flow before (pre) and after (post) activation/reduction. The concentrations of CH_4 and CO are shown alongside the temperature profile of the reactor cell. As expected, no catalytic activity is observed before activation, while clear CH_4 and CO formation is detected after activation.

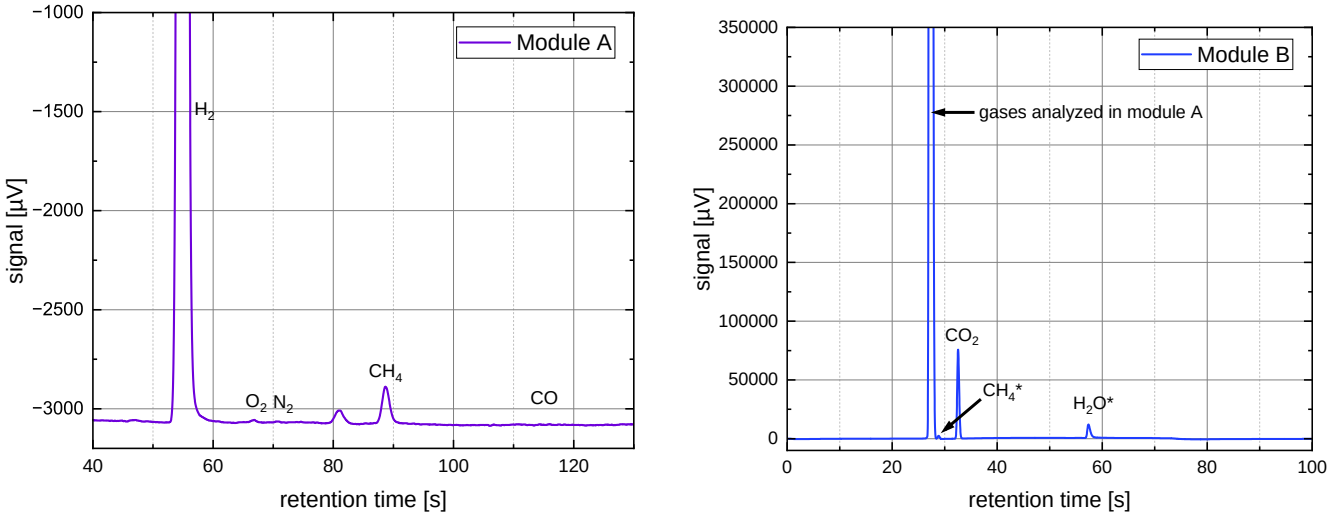

Fig. S23 Chromatograms from Module A (left, Rt-Molsieve 5 Å) and Module B (right, Rt-Q-Bond) recorded during operation of the 20-NiO/COK-12 catalyst at 400 °C under a H_2/CO_2 flow with a concentration ratio of 4:1. The GC was calibrated to quantify H_2, N_2, O_2, CO, and CH_4 in Module A, as well as CO_2 and C2–C4 hydrocarbons in Module B. * CH_4 and H_2O signals in Module B were detectable but not calibrated and therefore not quantified.

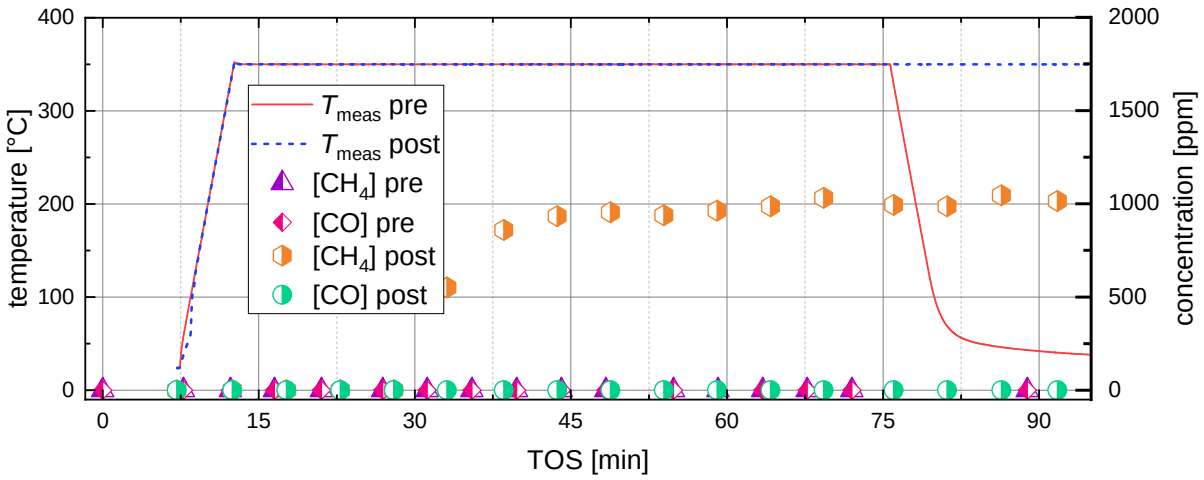

Fig. S24 Comparison of GC and temperature measurements of 20-NiO/COK-12 before(pre) and after(post) catalyst activation. The concentrations of CH_4 and CO are plotted over time-on-stream (TOS), alongside the corresponding temperature profile of the *in situ* cell. The data clearly demonstrate the emergence of catalytic activity – evidenced by increased CH_4 formation – only after activation, confirming the transformation of the catalyst into its active state.

7 Additional post-reduction operando experiments

Fig. S25 presents supplementary *operando* measurements of the 20-NiO/COK-12 catalyst after activation/reduction. To further evaluate the catalytic performance, the total gas flow was doubled at 350 °C (see total flow rate in panel (d)), followed by an increase in reaction temperature to 400 °C. In panel (c) of Fig. S25, the H_2/CO_2 ratio is shown to remain approximately 4:1 throughout the entire experiment.

As shown in Fig. S25(b), doubling the flow rate led to a decrease in the observed CH_4 concentration, which can be attributed to dilution of the product stream by the increased inflow of H_2 and CO_2. Conversely, increasing the reaction temperature to 400 °C resulted in a higher CH_4 concentration and CO_2 conversion, consistent with the endothermic nature of the methanation reaction and the enhanced reaction kinetics at elevated temperature.

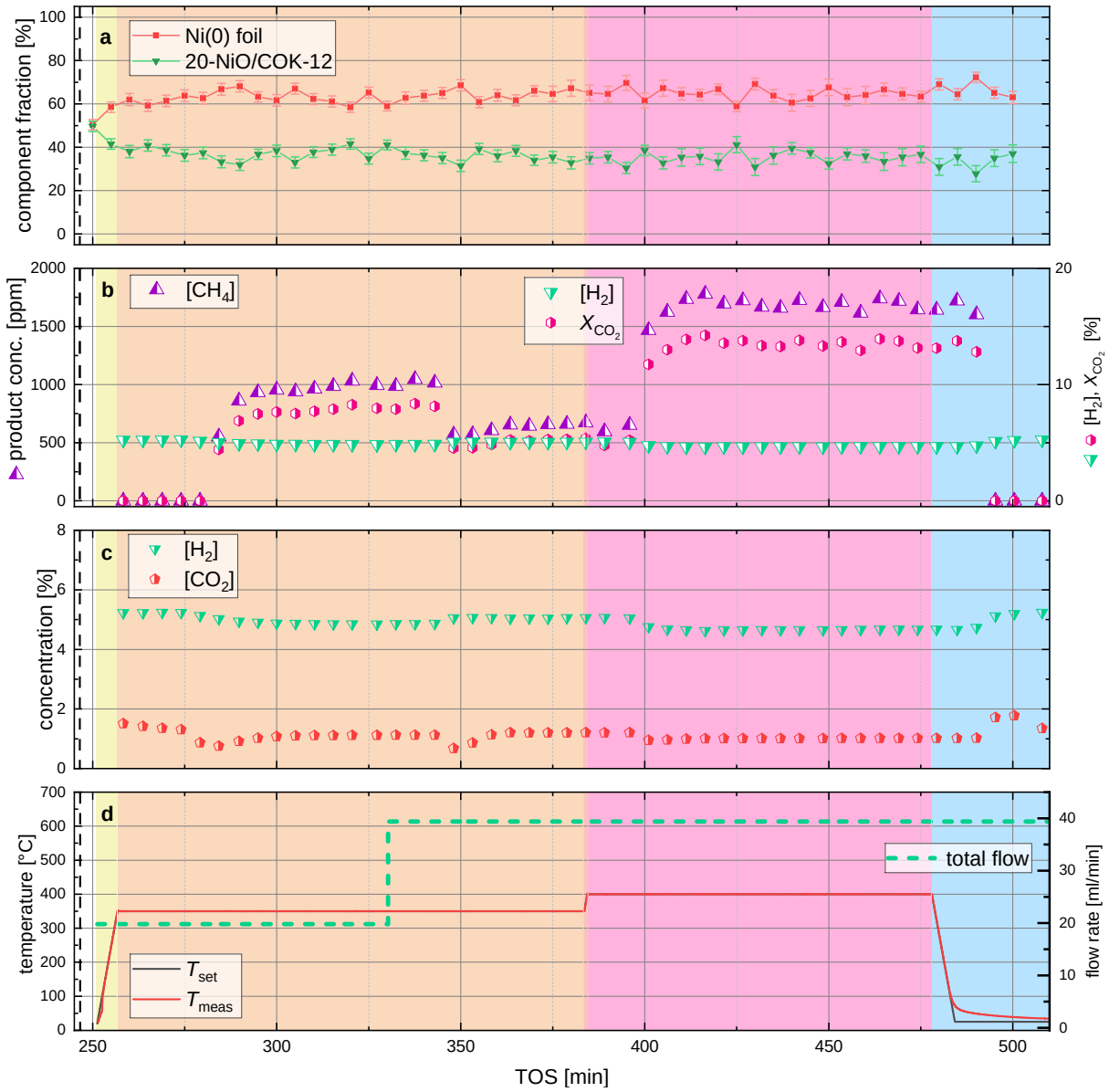

Fig. S25 Complete *operando* measurements of the 20-NiO/COK-12 catalyst after reduction. The top panel (a) displays the component fractions obtained from LCF of the XAS spectra; panel (b) shows the corresponding GC analysis of the reaction product and the CO_2 conversion together with the H_2 concentration; panel (c); and the bottom panel (d) presents the applied temperature profile and total flow rate. All data are displayed on a common cumulative time axis (time of stream, TOS), see pre-reduction and activation/reduction part in Fig. 6 of the main work.

Data availability

The raw data for this article – the raw and normalized XAS data – are available on Zenodo at `https://doi.org/10.5281/zenodo.17063731`.

Acknowledgements

This work was partially funded by the Deutsche Forschungsgemeinschaft (DFG German Research Foundation) under Germany's Excellence Strategy – EXC2008-390540038 – UniSysCat. Part of this work was funded by the German Federal Ministry of Education and Research in the framework of the project Catlab (03EW0015A) Peter Kraus acknowledges funding from the DFG (Project No. 490703766).

Notes and references

1 Bischoff B, Bekheet MF, Dal Molin E, Praetz S, Kanngießer B, Schomäcker R, et al. *In situ/operando* plug-flow fixed-bed cell for synchrotron PXRD and XAFS investigations at high temperature, pressure, controlled gas atmosphere and ultra-fast heating. Journal of Synchrotron Radiation. 2024 Jan;31(1):77-84. Available from: https://doi.org/10.1107/S1600577523009591.

2 Schlesiger C, Anklamm L, Stiel H, Malzer W, Kanngießer B. XAFS spectroscopy by an X-ray tube based spectrometer using a novel type of HOPG mosaic crystal and optimized image processing. Journal of Analytical Atomic Spectrometry. 2015;30:1080-5. Available from: https://doi.org/10.1039/C4JA00303A.

3 Schlesiger C, Praetz S, Gnewkow R, Malzer W, Kanngießer B. Recent progress in the performance of HAPG based laboratory EXAFS and XANES spectrometers. Journal of Analytical Atomic Spectrometry. 2020;35:2298-304. Available from: https://doi.org/10.1039/D0JA00208A.

4 V Hámos L. Röntgenspektroskopie und Abbildung mittels gekrümmter Kristallreflektoren. Naturwissenschaften. 1932 Sep;20(38):705-6. Available from: http://link.springer.com/10.1007/BF01494468.

5 Schlesiger CP. Röntgenabsorptionsspektroskopie im Labor [PhD thesis]. Technische Universität Berlin; 2019. Available from: https://depositonce.tu-berlin.de/handle/11303/9336.

6 Praetz S, Schlesiger C, Motz DA, Klimke S, Jahns M, Gottschalk C, et al. Can laboratory-based XAFS compete with XRD and Mössbauer spectroscopy as a tool for quantitative species analysis? Critical evaluation using the example of a natural iron ore. PLOS ONE. 2025 05;20(5):e0323678. Available from: https://doi.org/10.1371/journal.pone.0323678.

7 Air Liquide Deutschland GmbH. ARCAL® 15: 5% H_2 in Argon, Gas Cylinder 10 L, 200 bar (Ref. I2550S10R2A001). Düsseldorf, Germany: Air Liquide Deutschland GmbH; 2025. Gas mixture: H_2 (5 % ± 0.5 %) in Ar; conforming to DIN EN ISO 14175, Group R1 (R1-ArH-5). Accessed: 2025-10-06. https://de.airliquide.com/catalogue/arcaltm-15/arcal-15-zylinder-10l-200-bar/I2550S10R2A001.

8 Air Liquide Deutschland GmbH. Kohlendioxid (CO_2) Technisch, Gas Cylinder 10 kg, 49.5 bar (Ref. I5100S13R0A001). Düsseldorf, Germany: Air Liquide Deutschland GmbH; 2025. Purity: $CO_2 \geq 99.7$ %; impurities: $H_2O \leq 200$ ppm. CAS: 124-38-9. Accessed: 2025-10-06. https://de.airliquide.com/catalogue/kohlendioxid-technisch/kohlendioxid-zylinder-10kg/I5100S13R0A001.

9 Elam WT, Ravel BD, Sieber JR. A new atomic database for X-ray spectroscopic calculations. Radiation Physics and Chemistry. 2002;63(2):121-8. Available from: https://www.sciencedirect.com/science/article/pii/S0969806X01002274.

10 Doran A, Schlicker L, Beavers CM, Bhat S, Bekheet MF, Gurlo A. Compact low power infrared tube furnace for *in situ* X-ray powder diffraction. Review of Scientific Instruments. 2017 Jan;88(1):013903. Available from: https://pubs.aip.org/rsi/article/88/1/013903/367433/Compact-low-power-infrared-tube-furnace-for-in.

11 Schlicker L, Doran A, Schneppmüller P, Gili A, Czasny M, Penner S, et al. Transmission *in situ* and *operando* high temperature X-ray powder diffraction in variable gaseous environments. Review of Scientific Instruments. 2018 Mar;89(3):033904. Available from: https://pubs.aip.org/rsi/article/89/3/033904/368286/Transmission-in-situ-and-operando-high-temperature.

12 GmbH I. Micro GC Fusion 2-Module System; 2025. Accessed: 2025-09-22. https://www.inficon.com/en/products/gas-analysis/micro-gc-fusion-gas-analyzer. Available from: https://www.inficon.com/en/products/gas-analysis/micro-gc-fusion-gas-analyzer.

13 Rönsch S, Schneider J, Matthischke S, Schlüter M, Götz M, Lefebvre J, et al. Review on methanation – From fundamentals to current projects. Fuel. 2016;166:276-96. Available from: https://www.sciencedirect.com/science/article/pii/S0016236115011254.

14 Medina OE, Amell AA, López D, Santamaría A. Comprehensive review of nickel-based catalysts advancements for CO2 methanation. Renewable and Sustainable Energy Reviews. 2025;207:114926. Available from: https://www.sciencedirect.com/science/article/pii/S136403212400652X.

15 Zhang R, Wei A, Zhu M, Wu X, Wang H, Zhu X, et al. Tuning reverse water gas shift and methanation reactions during CO_2 reduction on Ni catalysts via surface modification by MoO_x. Journal of CO2 Utilization. 2021;52:101678. Available from: https://www.sciencedirect.com/science/article/pii/S2212982021002456.

16 Gili A, Schlicker L, Bekheet MF, Görke O, Penner S, Grünbacher M, et al. Surface Carbon as a Reactive Intermediate in Dry Reforming of Methane to Syngas on a 5% Ni/MnO Catalyst. ACS Catalysis. 2018;8(9):8739-50. Available from: https://doi.org/10.1021/acscatal.8b01820.

17 Gili A, Kunz M, Gaissmaier D, Jung C, Jacob T, Lunkenbein T, et al. Discovery and Characterization of a Metastable Cubic Interstitial

Nickel–Carbon System with an Expanded Lattice. ACS Nano. 2025;19(2):2769-76. Available from: https://doi.org/10.1021/acsnano.4c15300.

18 Jammaer J, Aerts A, D'Haen J, Seo JW, Martens JA. Convenient synthesis of ordered mesoporous silica at room temperature and quasi-neutral pH. J Mater Chem. 2009;19:8290-3. Available from: http://dx.doi.org/10.1039/B915273C.

19 Senocrate A, Bernasconi F, Kraus P, Plainpan N, Trafkowski J, Tolle F, et al. Parallel experiments in electrochemical CO_2 reduction enabled by standardized analytics. Nature Catalysis. 2024;7(6):742-52. Available from: https://doi.org/10.1038/s41929-024-01172-x.

20 Kraus P. dgpost: catalysis: common calculations in catalytic testing; 2024. Accessed: 2025-10-06. Available from: https://dgbowl.github.io/dgpost/main/apidoc/dgpost.transform.catalysis.html#dgpost.transform.catalysis.conversion.

21 Dimitrakopoulou M, Huang X, Kröhnert J, Teschner D, Praetz S, Schlesiger C, et al. Insights into structure and dynamics of (Mn,Fe)O_X-promoted Rh nanoparticles. Faraday Discussions. 2018;208:207-25. Available from: https://doi.org/10.1039/c7fd00215g.

22 Sigma-Aldrich. Nickel(II)-oxide; n.d. Green, 325 mesh, <44 µm, 99%, CAS-No: 1313-99-1. Catalog No. 436038, accessed May 2025. Available from: https://www.sigmaaldrich.com/DE/de/product/aldrich/399523.

23 Goodfellow. Nickel foil, 0.01 mm, 99.95 10x10 cm piece, free from pin-holes, catalog code LS83374 J V, manufacturer batch Ni000270/3. https://www.goodfellow.com/de/nickel-foil-light-tight-1000145319.

24 Zhao LD, Lo SH, Zhang Y, Sun H, Tan G, Uher C, et al. Ultralow thermal conductivity and high thermoelectric figure of merit in SnSe crystals. Nature. 2014 Apr;508(7496):373-7. Publisher: Nature Publishing Group. Available from: https://www.nature.com/articles/nature13184.

25 Li CW, Hong J, May AF, Bansal D, Chi S, Hong T, et al. Orbitally driven giant phonon anharmonicity in SnSe. Nature Physics. 2015 Dec;11(12):1063-9. Publisher: Nature Publishing Group. Available from: https://www.nature.com/articles/nphys3492.

26 Semiconductors D. SnSe Crystal; 2025. Accessed: 2025-09-22. https://2dsemiconductors.com/SnSe-Crystal/. Available from: https://2dsemiconductors.com/SnSe-Crystal/.

27 Aesar A. Zirconium Oxide, Catalyst Support (monoclinic phase), LOT P19G036; 2025. Accessed: 2025-09-24. Distributed by Thermo Scientific / Fisher Scientific. Available from: https://www.fishersci.de/shop/products/zirconium-oxide-catalyst-support-monoclinic-phase-thermo-scientific/11330468.

28 Ravel B, Newville M. ATHENA, ARTEMIS, HEPHAESTUS: Data analysis for X-ray absorption spectroscopy using IFEFFIT. In: Journal of Synchrotron Radiation. vol. 12; 2005. p. 537-41. Available from: https://doi.org/10.1107/S0909049505012719.

29 Praetz S, Johansen M, Kober D, Tesic M, Schlesiger C, Ravnsbæk DB, et al. Operando laboratory XAS on battery materials using the DANOISE cell in a von Hámos spectrometer. J Anal At Spectrom. 2025;40:2447-61. Available from: http://dx.doi.org/10.1039/D5JA00155B.

30 Wang T, Hu J, Ouyang R, Wang Y, Huang Y, Hu S, et al. Nature of metal-support interaction for metal catalysts on oxide supports. Science. 2024;386(6724):915-20. Available from: https://www.science.org/doi/abs/10.1126/science.adp6034.

31 Liu N, Chen B, Liu K, Qin R, Wang J, Zhang Y, et al. Ensemble Effect of the Nickel–Silica Interface Promotes the Water–Gas Shift Reaction. ACS Catalysis. 2023;13(11):7347-57. Available from: https://doi.org/10.1021/acscatal.3c00388.

32 Xie Y, Xia W, Jia S, Han S, Yao T, Fang M, et al. Silica-nickel catalyst interfaces promote highly efficient CO_2 electroreduction to CO with a wide potential range. Chemical Engineering Journal. 2023;461:141938. Available from: https://www.sciencedirect.com/science/article/pii/S1385894723006691.

33 Wagner CD, Gale LH, Raymond RH. Two-dimensional chemical state plots: a standardized data set for use in identifying chemical states by x-ray photoelectron spectroscopy. Analytical Chemistry. 1979;51(4):466-82. Available from: https://doi.org/10.1021/ac50040a005.